SANDIA REPORT
SAND2023-10724
Printed October 9, 2023

Sandia National Laboratories

MRT 7365: Power flow physics and key physics phenomena

Nichelle Bennett, Derek Lamppa, Andrew Porwitzky, Christopher Jennings, Dale Welch, Evstati Evstatiev, Clayton Myers, Kathy Chandler, Jacob Banasek, Sonal Patel, Eric Watson, David Yager-Elorriaga, Mark Savage, Mark Johnston, Mark Hess, David Rose, Michael Cuneo

Prepared by
Sandia National Laboratories
Albuquerque, New Mexico 87185
Livermore, California 94550

Issued by Sandia National Laboratories, operated for the United States Department of Energy by National Technology & Engineering Solutions of Sandia, LLC.

Available to DOE and DOE contractors from

U.S. Department of Energy
Office of Scientific and Technical Information
P.O. Box 62
Oak Ridge, TN 37831

Telephone: (865) 576-8401
Facsimile: (865) 576-5728
E-Mail: reports@osti.gov
Online ordering: http://www.osti.gov/scitech

Available to the public from

U.S. Department of Commerce
National Technical Information Service
5301 Shawnee Road
Alexandria, VA 22312

Telephone: (800) 553-6847
Facsimile: (703) 605-6900
E-Mail: orders@ntis.gov
Online order: https://classic.ntis.gov/help/order-methods

ABSTRACT

The Z accelerator at Sandia National Laboratories conducts z-pinch experiments at 26 MA in support of DOE missions in stockpile stewardship, dynamic materials, fusion, and other basic sciences. Increasing the current delivered to the z-pinch would extend our reach in each of these disciplines. To achieve increases in current and accelerator efficiency, a fraction of Z's shots are set aside for research into transmission-line power flow. These shots, with supporting simulations and theory, are incorporated into this Advanced Diagnostics milestone report.

The efficiency of Z is reduced as some portion of the total current is shunted across the transmission-line gaps prior to the load. This is referred to as "current loss". Electrode plasmas have long been implicated in this process, so the bulk of dedicated power-flow experiments are designed to measure the plasma environment. The experimental analyses are enhanced by simulations conducted using realistic hardware and Z voltage pulses. In the same way that diagnostics are continually being improved for sensitivity and resolution, the modeling capability is continually being improved to provide faster and more realistic simulations. The specifics of the experimental hardware, diagnostics, simulations, and algorithm developments are provided in this report.

The combined analysis of simulation and data confirms that electrode plasmas have the most detrimental impact on current delivery. Experiments over the last three years have tested the theoretical current-loss mechanisms of enhanced ion current, plasma gap closure, and Hall-related current. These mechanisms are not mutually exclusive and may be coincident in the final feed as well as in upstream transmission lines. The final-feed geometries tested here, however, observe lower-density plasmas without dominant ion currents which is consistent with a Hall-related current.

The picture of plasma formation and transport formed from experiment and simulation is informing hardware designs being fielded on Z now and being proposed for the Next-Generation Pulsed Power (NGPP) facility. In this picture, the strong magnetic fields that heat the electrodes above particle emission thresholds also confine the charged particles near the surface. Some portion of the plasmas thus formed is transported into the transmission-line gap under the force of the electric field, with aid from plasma instabilities. The gap plasmas are then transported towards the load by a cross-field drift, where they accumulate and contribute to a likely Hall-related cross-gap current.

The achievements in experimental execution, model validation, and physical analysis presented in this report set the stage for continued progress in power flow and load diagnostics on Z. The planned shot schedule for Z and Mykonos will provide data for extrapolation to higher current to ensure the predicted performance and efficiency of a NGPP facility.

CONTENTS

LIST OF FIGURES

SUMMARY

The Z accelerator at Sandia National Laboratories conducts z-pinch experiments at 26 MA in support of DOE missions in stockpile stewardship, dynamic materials, fusion, and other basic sciences. Increasing the current delivered to the z-pinch would extend our reach in each of these disciplines. To achieve increases in current and accelerator efficiency, a fraction of Z's shots are set aside for research into transmission-line power flow. These shots, with supporting simulations and theory, are incorporated into this Advanced Diagnostics milestone report.

The efficiency of Z is reduced as some portion of the total current is shunted across the transmission-line gaps prior to the load. This is referred to as "current loss". Electrode plasmas have long been implicated in this process, so the bulk of dedicated power-flow experiments are designed to measure the plasma environment. Three experimental series directly measure plasma densities in the final feed to the load. Four experiments infer the plasma densities and particle transport through measurements of current loss. The shots are summarized in Table 1-1.

The experimental analyses are enhanced by simulations conducted using realistic hardware and Z voltage pulses. In the same way that diagnostics are continually being improved for sensitivity and resolution, the modeling capability is continually being improved to provide faster and more realistic simulations. The specifics of the experimental hardware, diagnostics, simulations, and algorithm developments are provided in this report.

The combined analysis of simulation and data confirms that electrode plasmas have the most detrimental impact on current delivery. Transmission lines with low measured densities ($< 10^{16}$ cm^{-3}) suffer low losses. It is possible that even constriction points (localized small gaps) in the transmission line may have low plasma densities if the drift velocity is sufficient to sweep the plasma farther downstream.

Experiments tested the theoretical current-loss mechanisms of an enhanced ion current, plasma gap closure, and a Hall-related

current. These mechanisms are not mutually exclusive and may be coincident in the final feed as well as in upstream transmission lines. The final-feed geometries tested here, however, confirm the dominance of a lower-density plasma that is more consistent with Hall-related current and not gap closure or streamers. Likewise, the presence of ions may create bipolar currents upstream, but measurements disagree with a theoretical prediction of enhanced ion current loss.

The picture of plasma formation and transport formed from experiment and simulation is informing hardware designs being fielded on Z now and being proposed for the next-generation pulsed power (NGPP) facility. In this picture, the strong magnetic fields that heat the electrodes above particle emission thresholds also confine the charged particles near the surface. Some portion of the plasmas thus formed is transported into the transmission-line gap under the force of the electric field, with aid from plasma instabilities. The gap plasmas are then transported downstream by a cross-field drift, where they accumulate and contribute to a likely Hall-related cross-gap current.

While significant progress has been reported here, there are gaps remaining in our understanding that we have the tools in place to address. Questions include how much the current is lost in the

convolute and by what processes, how are particles/plasma sourced, how may loss be mitigated, and how do losses scale to higher currents. While we have confirmed that electrode plasmas are responsible for current loss, measuring the precise inventory has a been a decades-long pursuit in power-flow physics. Using our unmatched simulation capability, we have identified experiments that are sensitive to the electrode contaminant inventory with existing instrumentation. Diagnostics are being developed to measure ns-scale thermal desorption. Experiments designed to measure convolute losses, test new configurations, and scale to higher currents are scheduled for the coming year. A long-sought technique for mitigating current via *in situ* plasma cleaning is completing development on Mykonos for implementation on Z. Longer-term projects include measuring the emergence of electrode vaporization and simulating its impact on plasma in the vicinity of diagnostic apertures and the z-pinch load.

The achievements in experimental execution, model validation, and physical analysis presented in this report set the stage for continued progress in power flow and load diagnostics on Z. The planned shot schedule for Z and Mykonos will provide data for extrapolation to higher current to ensure the efficiency of a NGPP facility.

For reference, the milestone completion criteria for MRT 7365 are:

> Submit a technical report describing: (1) experimental progress for assessing power flow conditions at or near 20 MA, (2) our present understanding of the key physics phenomena responsible for electrode plasma formation and current loss at this scale, (3) comparison of power flow physics data (spectroscopy, velocimetry, particle diagnostics and others) and current loss results with multi-scale plasma models from CHICAGO plasma modeling, (4) provide a suite of verification problems that documents EMPIRE multi-scale plasma model performance in regimes relevant to a range of power flow applications at SNL, and (5) identify experimental and simulation gaps.

Tasks 1, 2, 3, and 5 are completed in this report. Task 4 is partially addressed in the Appendix and in a companion report.

NOMENCLATURE

AK gap anode-cathode gap

IDTL inductively driven transmission line

MITL magnetically insulated transmission line

NGPP Next Generation Pulsed Power

PDV photonic Doppler velocimetry

PIC particle-in-cell

SCL space-charge-limited

SVS streaked visible spectroscopy

1. INTRODUCTION

The *Z* accelerator at Sandia National Laboratories is designed to deliver up to 26 MA in 100 ns to drive a *z*-pinch load [63, 60] in support of a range of DOE missions. The loads, and the final section of the transmission line feeding them, vary in inductance and impedance which limits the peak current in ways that are straightforwardly calculable in transmission-line equations. These hardware geometries and dynamic changes in load inductance are captured in the transmission-line-circuit model of *Z* [29]. However, measurements show reductions in the current delivered to the load, referred to as "current loss", that there are not predicted geometrically or in traditional non-vacuum transmission-line theory [14, 43]. These are captured in the circuit model in an ad-hoc manner as dynamic resistances prescribed from fits to 52 shots on *Z*. This model is the workhorse for estimating current delivery for shot designs, but is less reliable for novel designs and extrapolation to higher currents. Traditional kinetic models of power flow include only surface emission of electrons and protons which are suitable only for kA-scale accelerators [12, 52], but do not provide insight to power flow physics at the multi-MA scale and do not reproduce the current loss on *Z* [47, 56, 57, 42, 55].

The FY23 Advanced Diagnostics (AD) milestone directly addresses this issue. A coordinated campaign of experiments, code development, and theory has advanced our understanding of power flow and current loss in transmission lines operating above 20 MA. Dedicated power-flow shots are fielding new diagnostics [48, 46] to measure the plasma environment and current delivery. Code developments in the hybrid particle-in-cell (PIC) code CHICAGO enable more realistic simulations of these shots. The validated simulations and data are interrogated to identify the key physics phenomena responsible for electrode plasma formation and reduction in load current.

The progress of this coordinated campaign is described in this report. The power-flow shot series on *Z* are designed to test competing theories for current loss and to diagnose the electrode plasmas that are inevitable in multi-MA *z*-pinch drivers. These power-flow shot designs and key measurements are presented in Sec. 3 and summarized in Table 1-1.

The simulations of these shots are conducted in CHICAGO with newly-developed algorithms for capturing the physical phenomena impacting multi-MA accelerators [72]. A brief survey of the particles and emission processes that are accessed at the MA scale is provided in Sec. 2 for reference. Code improvements and the simulation technique are detailed in Sec. 4. The integrated data and simulation analysis is presented in Sec. 5. Section 3 describes what is unique to each shot series while Sec. 5 describes the physical phenomena these shots collectively uncover.

This combined shot analysis has enabled us to distinguish the dominant current loss mechanism in *Z*'s final feed from among the competing theories. The theories include an enhanced ion current [29, 68, 55], higher-inductance transmission lines [24], plasma gap closure [24], and rapid transitions from radial to coaxial in the transmission line (90-degree bends). The simulations aid in data analysis and shed light on the physics that is not diagnostically accessible. This allowed us to identify yet another loss mechanism, a Hall-conductivity-related current, that is related to inductance [5]. The current-loss mechanisms are described in more detail in Sec. 5. Our present understanding of electrode plasma formation and current loss at the multi-MA scale is presented

Experiment	Objective	Section	Summary Conclusions
Power Flow Diagnostics	characterize gap plasmas	Sec. 3.1	plasma density in the MITL gap is 10^{17} cm^{-3} until after peak current
Power Flow 18a	evaluate current loss versus gap width and in 90° MITL bends	Sec. 3.2	the length of MITL increases current loss, no impact from gap width or bend
Power Flow Validation	evaluate current loss in small gaps and 90° MITL bends	Sec. 3.3	plasma clearing is observed, no evidence of full gap closure
Power Flow Scaling	evaluate current loss at NGPP **E** and **B** field conditions	Sec. 3.4	current transport is lossless through 2-mm gap with bends
Inverted Convolute	evaluate enhanced ion current loss mechanism	Sec. 3.5	no evidence of enhanced ion current
Reverted Convolute	evaluate enhanced ion and Hall-related current loss mechanism	Sec. 3.5	loss agrees with predicted Hall-related current for moderate level of surface contaminants
MagLIF with debris mitigation	evaluate impact of debris shields	Sec. 5.1	debris shields do not reduce current

Table 1-1 The individual experiments supporting the Advanced Diagnostics and Power Flow campaign.

in Sec. 6. The gaps in our understanding and further areas of investigation are summarized in Sec. 7.

Finally, because the *Z* plasma environment is extreme, the codes that simulate it must capture surface physics and be able to evolve plasmas at densities greater than 10^{17} cm^{-3}, which is stressing for PIC codes. Exemplar problems are provided in Appendix 8 as minimum tests of the required code capability.

2. SURVEY OF PARTICLES AND EMISSION IN HIGH-CURRENT TRANSMISSION LINES

The electrode operating conditions in pulsed-power z-pinch drivers range from near vacuum to charged-particle emission (no plasmas), then to surface/bulk contaminant desorption (low-density plasmas), and ultimately melt (solid-density plasmas). A transmission-line segment will transition through some or all of these conditions over the course of a pulse. Further, this range of conditions exists simultaneously at different radii or local current density.

This leads to the complicated bound and free current transport referred to as power flow. The cartoon in Fig. 2-1 illustrates the progression of particle emission with pulse rise in a low-impedance transmission line. Electrons are the most mobile particles and may be liberated through tunneling at low energies, which is the description for high-impedance transmission lines [21, 44]. In accelerators, electron emission is still initiated by an electric field threshold, however currents are sufficiently high that the quantum mechanical description gives way to one governed by tenuous cathode plasmas. The electron current through the surface is self-limited by the opposing space charge it establishes.

Protons are the next most loosely bound particles and are emitted from the anode when, with continued pulse rise, the surface temperature exceeds a threshold. The measured threshold of 700 K [58, 17] is indicated in Fig. 2-1. Proton emission is similarly self-limited by space charge. These vacuum to electron and proton emission stages are well-understood [14, 15, 43, 38] and previously modeled [11, 12, 52].

The pulse rises continues to heat the electrodes, desorbing the more tightly bound particles. Liberated neutral molecular water and other contaminants fragment and ionize, forming a surface plasma which increases in density throughout the pulse, or until their inventory is depleted. This stage is marked by increasing particle density and surface temperatures, denoted by 10^{16} cm^{-3} and 11000 K in Fig. 2-1.

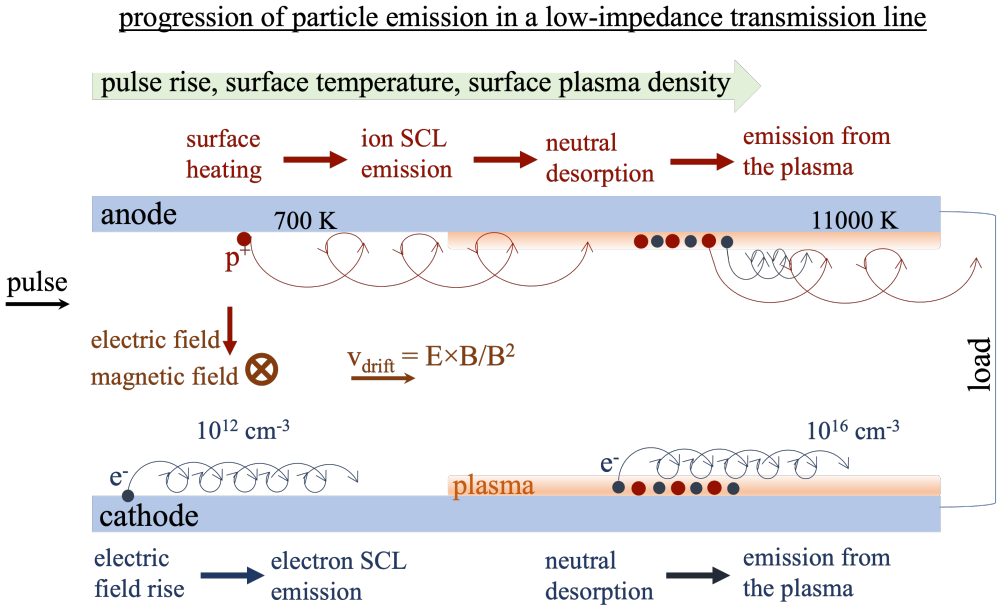

Figure 2-1 The progression of particle emission with pulse rise in a low-impedance transmission line. The pulse rise increases the electric field (inductively in a near short-circuit *z*-pinch load) and the electrode surface temperature. Electrons are emitted from the cathode after the electric field threshold is exceeded. Protons are emitted from the anode after a temperature threshold is exceeded. Eventually, neutral particles are thermally desorbed from both electrodes and ionize to form a surface plasma that dominates the particle environment.

3. POWER FLOW EXPERIMENTAL CAMPAIGN

Current loss on *Z* occurs routinely interior to the region in which particles are emitted from the electrodes. The size of this region is small compared to the overall size of *Z*. This is illustrated in Fig. 3-1 which details *Z*'s main components. Power is supplied by 36 pulsed-power modules which are connected in parallel to four radial magnetically insulated transmission lines (MITLs), labeled "outer MITLs" in Fig. 3-1. Currents from the outer MITLs are combined within a double post-hole convolute and transferred to a single radial "inner" MITL that transports the full current to the load. These last three sections are included in the small volume located within the dashed lines in Fig. 3-1. This volume is where the current loss occurs in normal operation and where our shot hardware is tailored to study power flow.

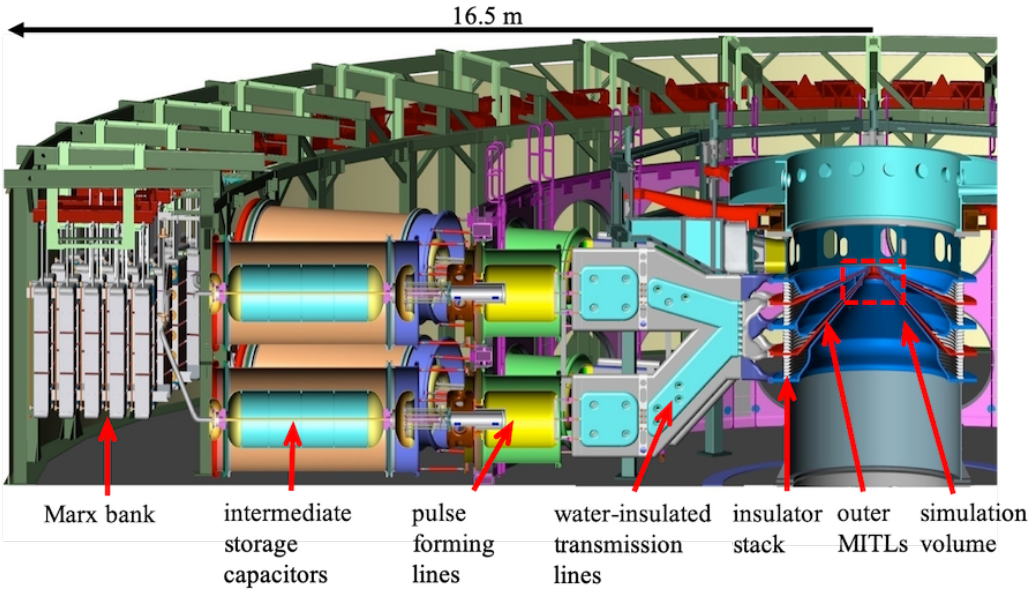

Figure 3-1 Cross section of Sandia's *Z* machine [62, 59]. The region of interest for plasma formation and current loss is outlined by the dashed red lines.

More details of this volume are given in Fig. 3-2. This figure is useful for orienting the engineering drawings and simulation renderings that follow. The cross-sectional view illustrates how the post-hole convolute electrically connects the anode plates of the four outer MITLs (shown in blue). Twelve azimuthally arrayed posts attach to the three anode plates and pass through holes in the cathode plates (shown in red). The inner MITL is the final line that carries the full current to the load. This report concentrates on inner MITL losses. Studies of convolute losses are in progress.

Each *Z* shot has an inner MITL that is tailored for the load. For power flow studies under this AD milestone, the inner MITLs are designed to increase sensitivity to the plasma conditions or current-loss theory under test. The shot hardware, motivation, and key diagnostics are described here for six distinct shot series, executed over the last three years.

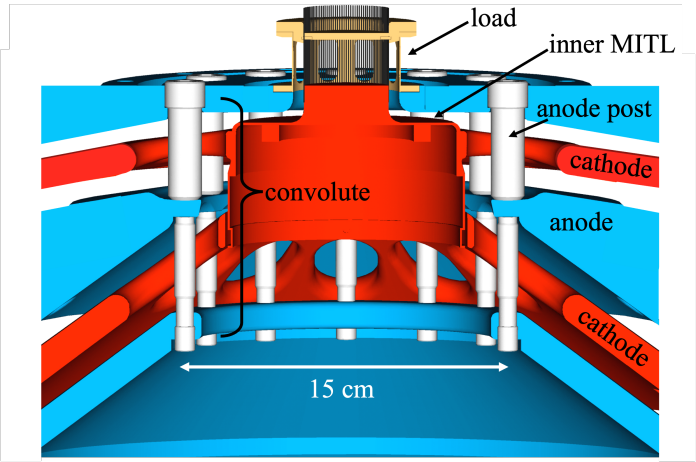

Figure 3-2 A cross section of the Z machine outer MITLs, ∅15cm double post-hole convolute (current adder), and inner MITL [63].

3.1. Power Flow Diagnostics

The hardware platform labeled "Power Flow Diagnostics" was developed to accommodate multiple plasma diagnostics that each require line-of-sight access into the inner MITL. The platform is illustrated in Fig. 3-3. The diagnostic windows in the anode span 270° in azimuth, creating unobstructed lines of sight for diagnostics but also azimuthal asymmetries in the electric and magnetic fields. Such asymmetries are a risk typically not tolerated by load designers, therefore, measurements of the inner-MITL plasma require these dedicated shots.

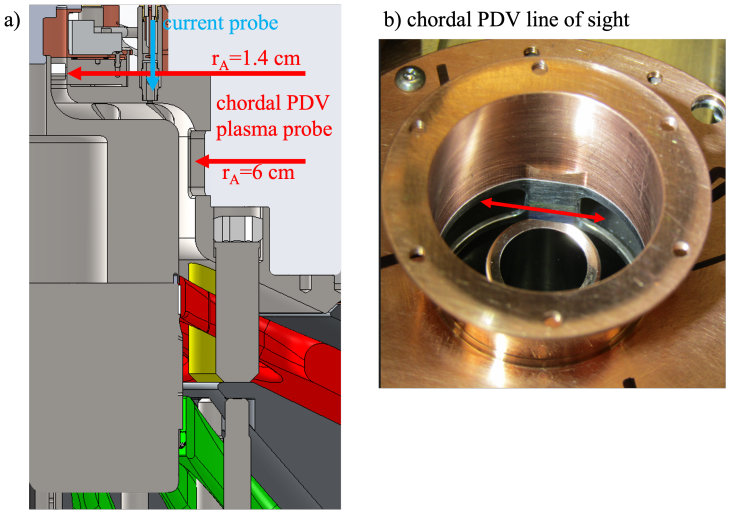

Figure 3-3 a) Engineering drawing of the Power Flow Diagnostics inner MITL with the chordal PDV probe locations labeled by anode radius (r_A). This series is fielded on the 15-cm-diameter convolute. b) Image of the interior of the anode hardware identifying the chordal PDV line of sight.

The plasma diagnostics all operate in the visible portion of the spectrum, unlike those fielded for

analyzing the z-pinch [31, 69]. These diagnostics include a framing camera for self-emission [74], a fiber array for time-integrated spectroscopy (previously reported in Ref. [34]), and two fibers for chordal photonic Doppler velocimetry (PDV) [20, 19]. The latter measures plasma density in the middle of the anode-cathode (AK) gap at two locations. The PDV data are analyzed in conjunction with simulation (in Sec. 5.3) to increase our understanding of the contaminant plasma inventory, plasma transport, and the likelihood of gap closure.

PDV is a fiber-based interferometry technique that infers a plasma density from its impact on the index of refraction [18]. Previous measurements on Z are described in detail in Refs. [20] and [48]. Assuming the plasma density (n_p) is uniform, it is calculated using

$$n_p = \frac{2n_c}{L}\int_{t_0}^{t_f} v(t)dt, \tag{1}$$

where n_c is the critical plasma density, L is the laser path length, v is the apparent velocity, and t_0 and t_f are the limits of integration. In an unmagnetized plasma, the critical density derives from the plasma frequency (ω_p) above which an electromagnetic wave of frequency ω can not propagate, or $\omega_p(n_c) = \omega$. The path length L is assumed to be the chordal distance interior to the anode. The choice of t_0 is complicated by the radiation signal imposed on $v(t)$ and impacts the calculated density. Three values of t_0 are used in the calculated data in Figs. 3-4 and 3-5.

The two PDV lines of sight in Fig. 3-3 enable plasma measurements at two positions along the inner MITL, which correspond to different surface temperatures. Two chords are recorded near $r_A = 6$ cm and plotted in Fig. 3-4. At this position, the cathode surface reaches ~ 1000 K at peak current and thermal emission is predicted to occur at ~ 3045 ns, based on the measured load current [4]. The integration intervals starting from $t_0 = 3030$ and 3040 ns are more physical than $t_0 = 2960$ ns, and are consistent with this predicted emission time. Neither plot shows measurable density away from the electrode surfaces until ~ 3060 ns.

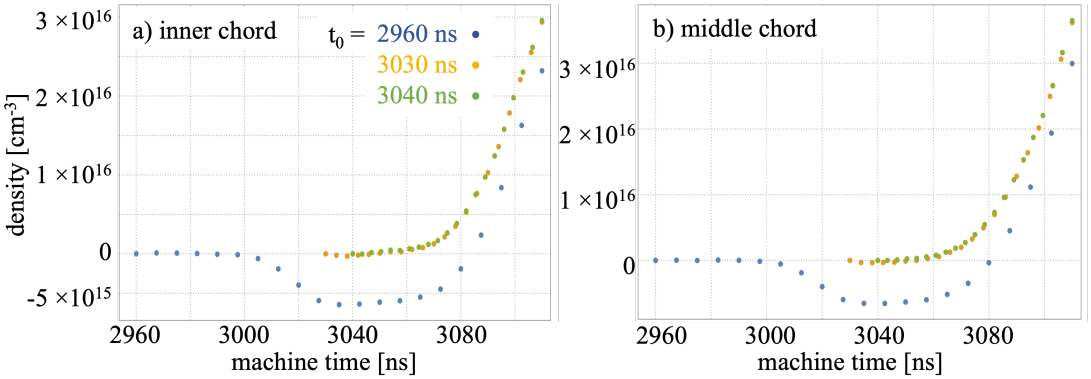

Figure 3-4 The plasma density for Power Flow Diagnostics shot z3454 (Fig. 3-3) measured using chordal PDV at $r_A = 6$ cm. Three values are sampled for the lower limit of integration ($t_0 = 2960$, 3030, and 3040 ns) in Eq. 1.

The densities in Fig. 3-5 are recorded closer to the axis ($r_A = 1.4$ cm) where the cathode temperature exceeds the thermal emission threshold by 3010 ns. The density at at 3100 ns is $\sim 2 \times 10^{16}$ cm^{-3} which appears similar to the measurements at $r_A = 6$ cm, but the timings,

alignment, and peak currents are different. The impact of magnetic confinement in limiting the diffusion into the gap is discussed in in Sec. 5.3.

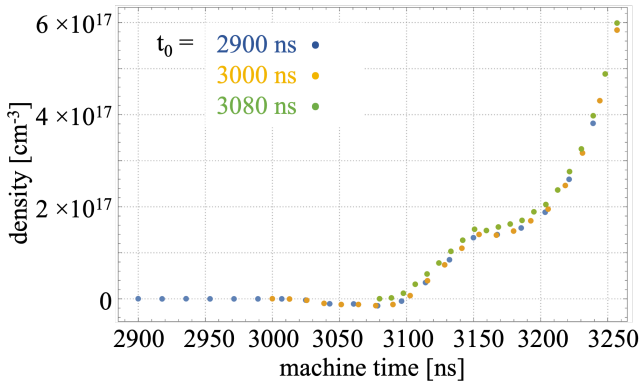

Figure 3-5 The plasma density for Power Flow Diagnostics shot 3776 (Fig. 3-3) measured using chordal PDV at $r_A = 1.4$ cm. Three values are sampled for the lower limit of integration ($t_0 = 2900$, 3000, and 3080 ns) in Eq. 1.

3.2. Power Flow 18a

The "Power Flow 18a" shots were designed to deliver unambigous load currents from a static load for model testing. It was fielded on a variant of the current adder region in which the posts are located at a diameter of 31 cm (∅31cm convolute). The inner MITL hardware is illustrated in Fig. 3-6, which shows the location of the load current probe.

Having validated the simulation code in this regime [71, 4], the load currents provide insights on the impact of near 90-degree bends in the inner MITL and the mechanisms responsible for current loss in the convolute and inner MITL. The analysis of the 90-degree bend is included in the larger analysis of electrode plasma formation and transport presented in Sec. 5.3. The load current analysis supports our present understanding of the Hall-conductivity related current loss discussed in Sec. 5.4.

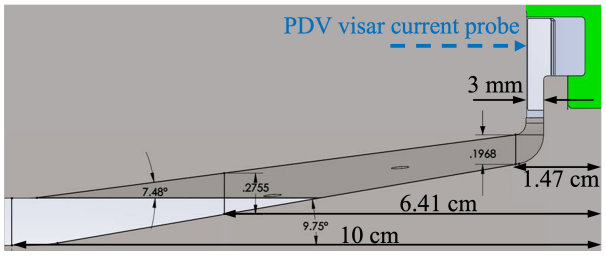

Figure 3-6 Engineering drawing of the Power Flow 18a inner MITL hardware. This shot was fielded on the 31-cm-diameter (∅31cm) convolute.

3.3. Power Flow Validation

The "Power Flow Validation" shot series was designed to test the *Z* machine's ability to deliver > 20 MA through AK gap widths of 2 mm or less. This is to verify the result in Ref. [64] which found that MITL gaps of 1 and 2 mm resulted in current loss to wire-array loads. The AK-gap scan is repeated here with an imploding-liner load but with direct measurements of the load current replacing the inferred currents from the x-ray yields. The total inductance is held constant by increasing the length of the "return can" encompassing the load in conjunction with the reducing the minimum AK gap width of a coaxial MITL segment at $r = 1$ cm. This is illustrated in the hardware drawings in Fig. 3-7a-d which show the four gaps tested: 1, 2, 3, and 6 mm.

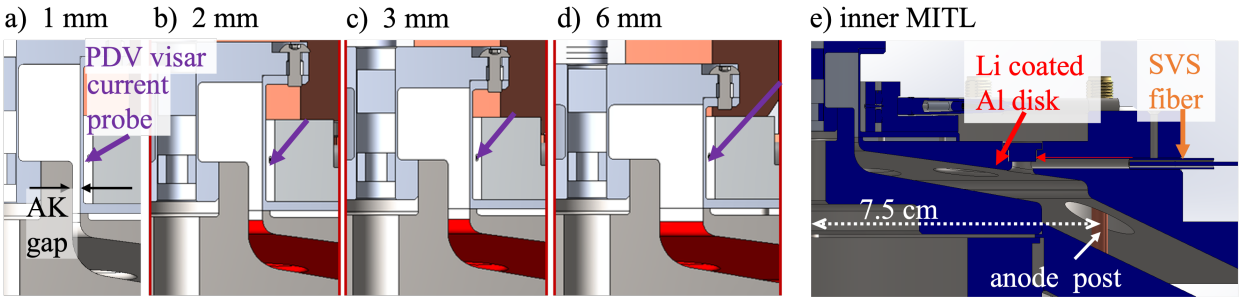

Figure 3-7 a-d) The four inner MITL configurations for the power-flow validation shot series labeled by AK gap width. e) The inner MITL for this series with SVS recording the anode at outer radius.

The reconstructed load currents for the four AK gap widths are plotted in Fig. 3-8. The 6, 3, and 2-mm-gap currents are the same within measurement error. Unlike Ref. [64], this overall MITL shape does not distinguish between gaps. We note that this MITL is a reasonable surrogate for the wire array shots in Ref. [64], with a 1-cm-radius cathode downstream from a 90-degree bend. These currents are compared to simulation and used to motivate the Hall-conductivity-related loss discussed in Sec. 5.4.

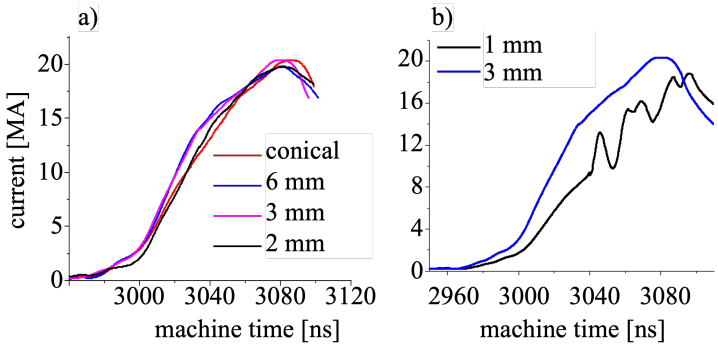

Figure 3-8 The measured load currents from the Power Flow Validation AK gap scan with imploding loads. The load current from a conical MITL with the same inductance and imploding load is included for reference.

The load current for the 1-mm gap, plotted in Fig. 3-8b, does show more structure and more loss over the pulse than the other gaps. The 3-mm current is included in Fig. 3-8b for comparison. The higher loss at 1 mm, and the structures observed in the pulse, may be attributed to magnetic clearing, which is described in Sec. 5.3.

This platform also provided useful information on power-flow and plasma conditions upstream. The inner MITL, shown in Fig. 3-7e, is similar to the Power Flow 18a geometry (Fig. 3-6), but shorter for fielding on the standard 15-cm-diameter convolute. Both shot series demonstrate the impact of a 90-degree bend in the inner MITL. The analysis of plasma transport through such bends, as well as through the minimum AK gaps. is discussed in Sec. 5.3.

The plasma density upstream in the inner MITL is inferred from Streaked Visible Spectroscopy (SVS). A fiber probe records the spectrum over time from a Li coated Al disk on the anode at $r = 5$ cm, as shown in Fig. 3-7e. From fits to the Li I and Hα lines (Fig. 3-9a), the surface density ranges from 1 to 7×10^{17} cm^{-3} for all shots (Fig. 3-9b), higher than the gap densities observed with chordal PDV.

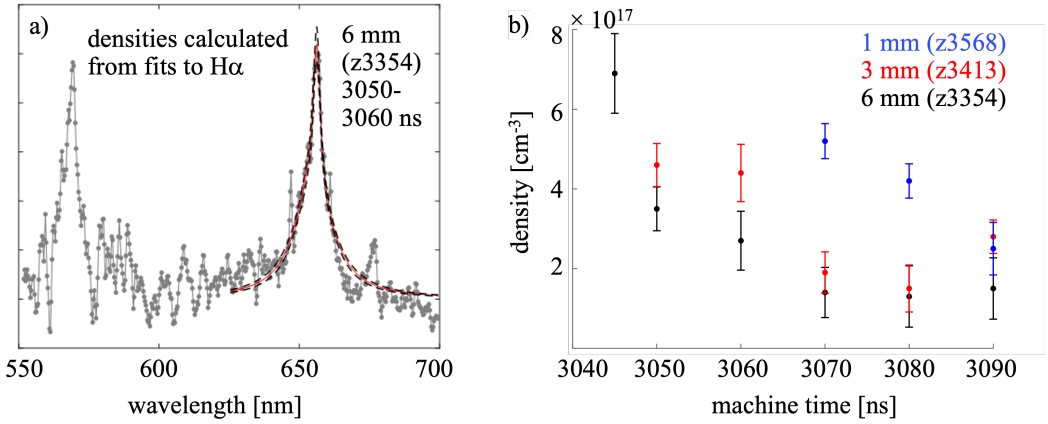

Figure 3-9 The streaked visible spectroscopy (SVS) from the Power Flow Validation shot series. The SVS fiber views the anode surface near $r = 5$ cm, shown in Fig. 3-7e. a) A snapshot of the spectrum is fit to Hα emission to estimate the plasma density. b) The reconstructed anode plasma densities from the AK gap scan.

Particle fluences in the convolute were measured using Faraday cups embedded in the anode posts. Eleven unfiltered Faraday cups were arrayed azimuthally on the downstream surface of the posts and biased to collect electrons and negative ions. They are also sensitive to photons. The shot-averaged data are plotted in Fig. 3-10.

3.4. Power Flow Scaling

The "Power Flow Scaling" platform is intended as a 20-MA design with the equivalent field and current density conditions of 40 to 60-MA drivers, such as a NGPP facility [45]. Figure 3-11 shows this scaling is achieved by the relation $j = I/r$, where j is the lineal current density, I is the

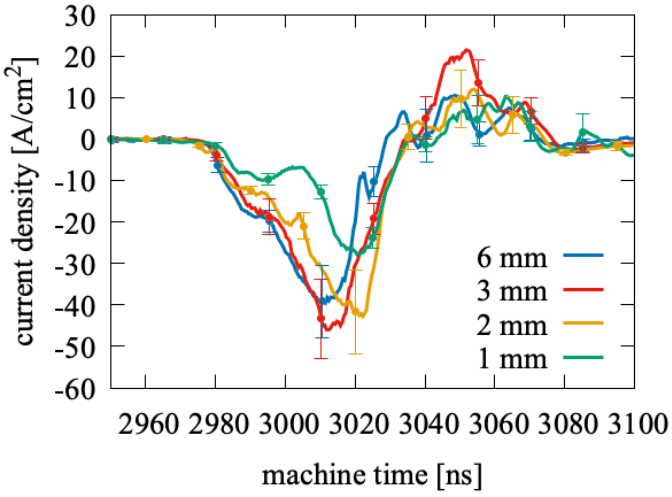

Figure 3-10 Shot-averaged Faraday cup signals embedded in the anode posts for the Power Flow Validation AK gap scan. The current density represents negatively charged particles or photons.

current, and r is the distance fro the axis in a radial transmission line. For a fixed impedance and AK gap width, the same relation holds for the axial electric field E_z.

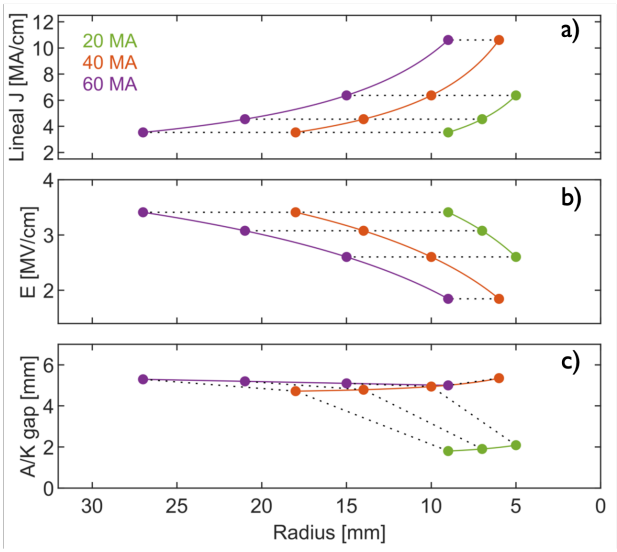

Figure 3-11 The scaling of the current density (j) and electric field (E_z) a a function of radius in a transmission line.

In the Power Flow scaling design, the segment of the radial transmission line used for comparison is labeled “Scaled transmission line” in Fig. 3-12. A 2-mm AK gap and static load is shown and was the first shot in this series (z3537). A point-probe visar current probe was fielded on the outer radius of the anode “return can”. Four Z line visar probes were arrayed radially along the outer axial wall of the anode can.

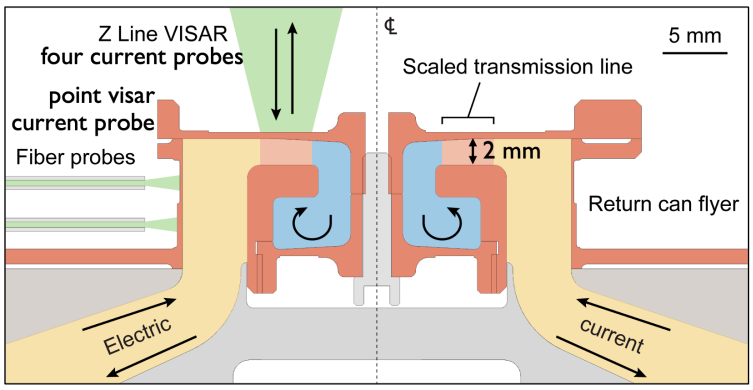

Figure 3-12 The Power Flow Scaling load design and diagnostics. Current is measured by point visar on the outer radius of the "return can" and by four *Z*line visar probes at top axial position.

The reconstructed currents from these five probes are plotted in Fig. 3-13a. This inner MITL was fielded a second time with an (under-driven) imploding load. The currents from this second shot (z3617) are plotted in Fig. 3-13b. Both of these 2-mm-gap shots appear lossless. This agrees with the simulation results presented in the context of plasma transport and current loss in Secs. 5.3 and 5.4.

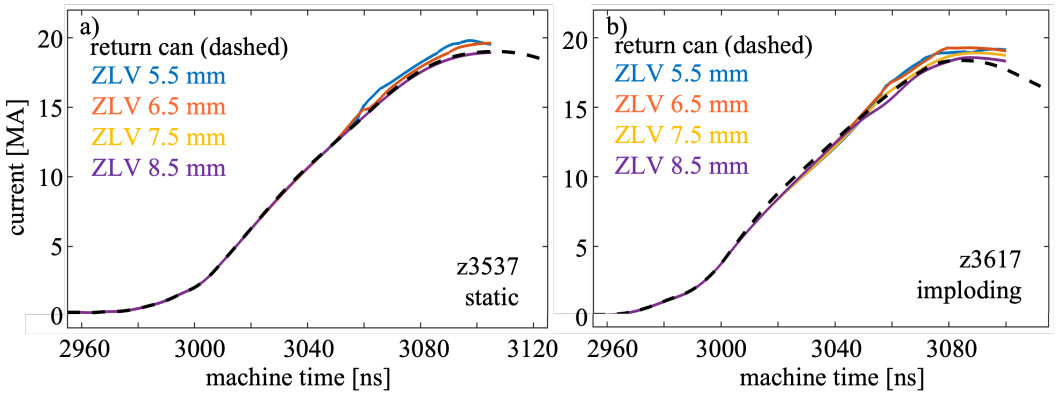

Figure 3-13 The reconstructed currents from the Power Flow Scaling shot with a) a 2-mm AK gap and a static load and b) a 2-mm AK gap and an imploding load. The locations of the current probes are shown in Fig. 3-12. The imploding liner is located at the innermost radius. Note the z3617 pulse is ~ 15 ns later than z3537.

3.5. Reverted Convolute

The "Reverted Convolute" platform was developed as a follow-on to the "Inverted Convolute". Both were conceived to test the enhanced ion current loss mechanism [68, 55]. In this theory, the particle current entering the inner MITL from the convolute is dominated by electrons. Their negative space-charge would draw more positive ions from the anode than the applied fields

alone, leading to positive-ion-dominated loss currents. Faraday cups were fielded to capture these positive ions as they reach the cathode. As "Inverted Convolute" suggests, the polarity is inverted from normal (negative polarity) operation to position the Faraday cups on an exterior cathode. This relocated the current probes to the interior of the inner MITL, which is a challenging radiation environment. The Inverted Convolute shots concluded with very preliminary Faraday cup ion current densities of ~ 300 A/cm^2, poor IDTL current signals due to electron bombardment of the detectors, and no evidence of enhanced ion current.

The Reverted Convolute reverts to the standard Z polarity, restoring the current probes to the exterior of the inner MITL. The inner MITL geometry and probe locations are illustrated in Fig. 3-14. To keep the Inverted Convolute's inductance profile, the inner MITL is an extended line similar to those fielded on Z's dynamic materials experiments. The AK gap in the coaxial segment is a scant 3 mm, while the length of this segment exceeds 18 cm.

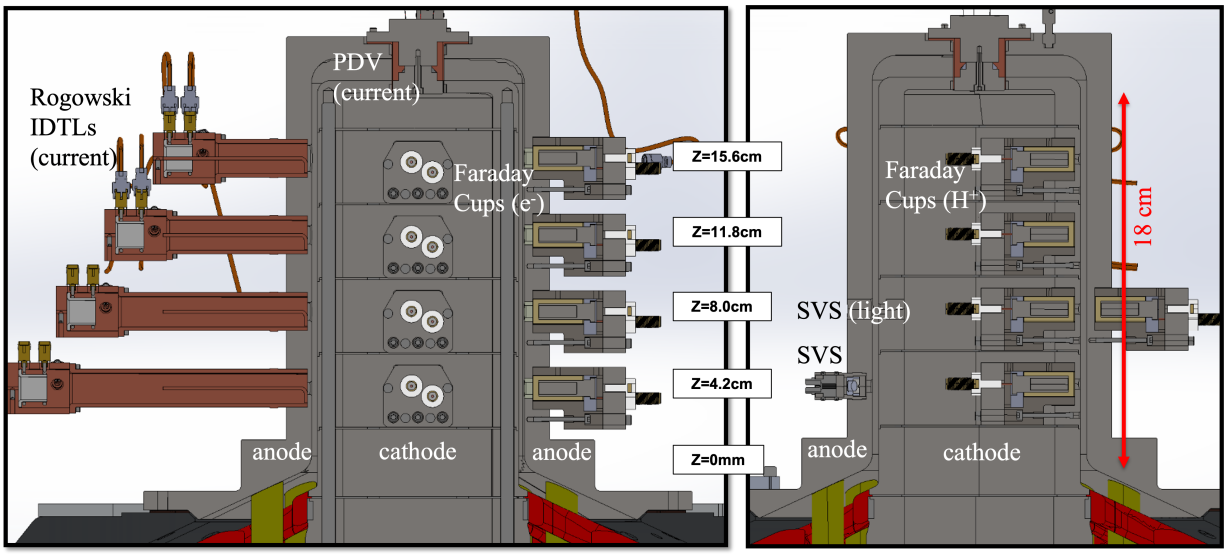

Figure 3-14 The Reverted Convolute inner MITL design and diagnostics. Current is measured at five locations: four Rogowski IDTL probes [46] along the 18-cm-long inner MITL and a PDV probe [19] at the MITL termination.

The pre-shot simulations of the Reverted Convolute (discussed in Sec. 5) identified this platform as uniquely suited to test the Hall-conductivity related current loss mechanism. The two subsequent shots verified The Hall-related current loss. The MITL currents from the first shot are plotted in Fig. 3-15. The "stack" current is measured at the insulator stack in Fig. 3-1 and represents the total current supplied to the inner MITL. The Rogowski IDTL currents are labeled by their position in Fig. 3-14. Current is steadily lost along the MITL from the stack through through the IDTLs to the PDV load current. The stack and load currents for both shots are plotted in Fig. 3-16.

The SVS diagnostic fielded at three axial positions were focused on the cathode surface in the second shot (z3873). All show coincident continuum emission beginning at 3010 ns machine time. The temporal responses at the 550 and 740 nm lines in the continuum are plotted in Fig. 3-17. To ensure that the signal is from photons and not electron bombardment of the lenses,

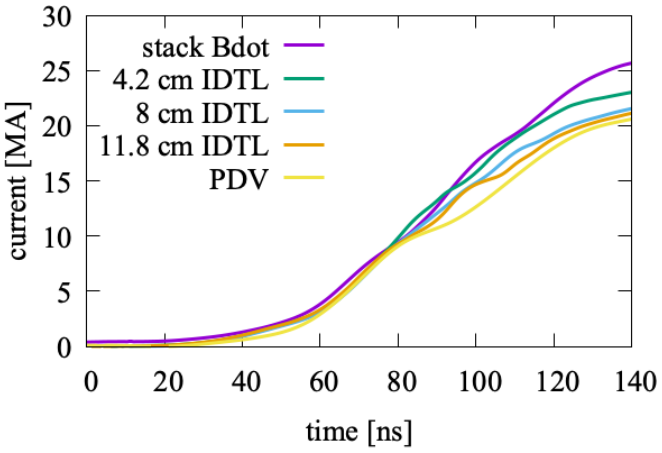

Figure 3-15 The Reverted Convolute measured Rogowski IDTL currents and the calculated PDV current for shot z3775. The probe locations are labeled in Fig. 3-14. The current at the stack (purple) is the total injected current into the inner MITL from the BERTHA-circuit [29] translated stack current. The PDV current is located at the inner radius in Fig. 3-14. This large loss was designed to identify the loss mechanism.

one of the probes is shielded by a 1 T magnet to divert charged particles. The unmagnetized and magnetized signals in Fig. 3-17 are consistent.

The current densities calculated from the anode-side Faraday cups fielded on the second shot (z3873) are plotted in Fig. 3-18. The signals arrivals corroborate the timing of cathode breakdown and cathode plasma formation early in the pulse.

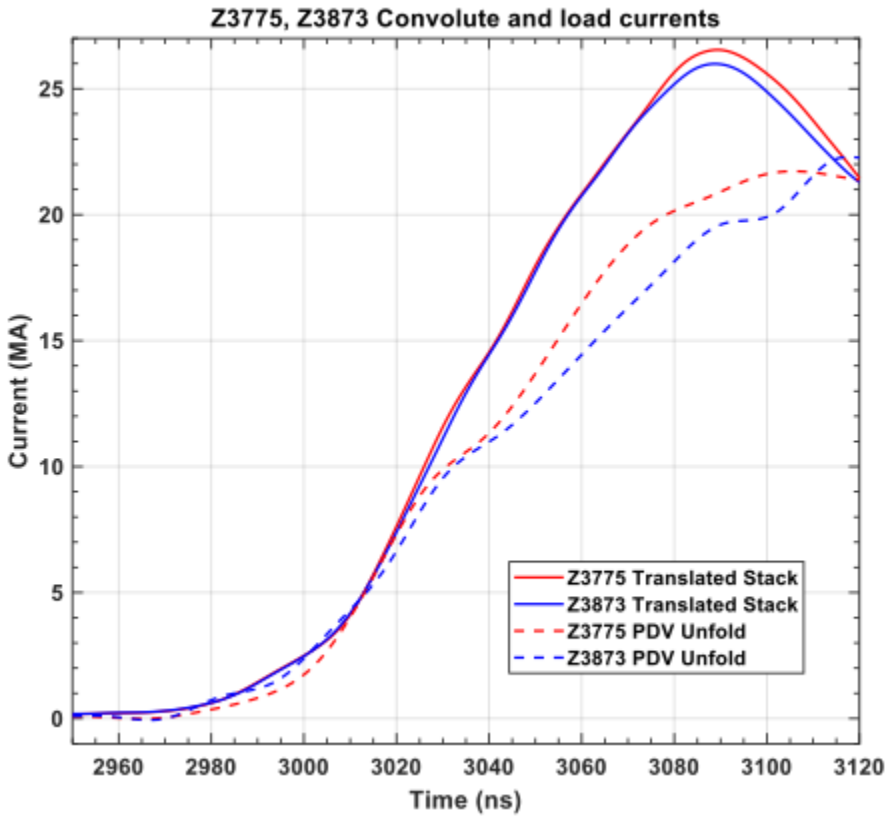

Figure 3-16 The currents into the MITL (stack) and at the load (PDV) for the Reverted Convolute shots z3775 and z3873. Large losses were deliberately and reproducibly created to distinguish the loss mechanism unambiguously.

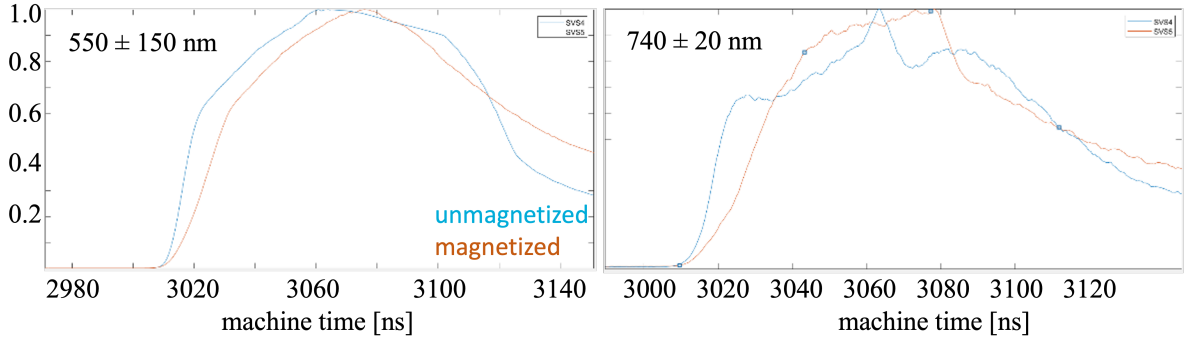

Figure 3-17 Streaked visible spectroscopy responses at 550 and 740 nm in the Reverted Convolute (Fig. 3-14), indicating cathode plasma emission early in the pulse.

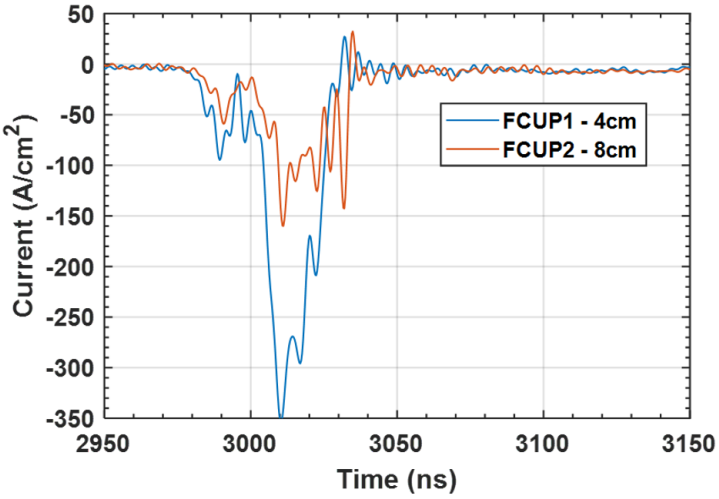

Figure 3-18 The Reverted Convolute Faraday cup signals. The probe locations are labeled in Fig. 3-14. Cathode plasmas are present as early as 2980 ns (machine time).

4. SIMULATIONS

Simulations are powerful tools for designing shot hardware, predicting its electrical behavior pre-shot, interpreting diagnostics post-shot, and generally disentangling the physical processes involved. For this reason, significant improvements were made to our primary power-flow code CHICAGO to enable faster and more detailed models of each of the experimental campaigns described in Sec. 3. The resulting combined analysis of data and simulation has advanced our understanding of power flow physics in *Z* and at the multi-MA scale, in general. This is presented in Sec. 5. Here, we outline the code requirements for modeling *Z*, important code advances (Sec. 4.1-4.3), and how *Z* simulations are constructed (Sec. 4.4).

The pulsed-power transmission line environment is defined by its transition from vacuum operation to low-density ($10^{12} - 10^{15}$ cm^{-3}) charged particle currents. This physical regime is the ideally suited for particle-in-cell (PIC) codes, which may propagate electromagnetic fields in vacuum but may also self-consistently propagate relativistic charged particles, which are both influenced by and modify these fields. As the current density increases in pulsed power systems, the apex being the *Z* machine, electrode surface plasmas impact system efficiency (current loss) and must also be modeled.

This last requirement is stressing for a PIC code because the electron motion in *Z*'s extreme magnetic fields, and in the presence of plasma, must be resolved. The electron cyclotron motion limits the width of current sheaths and the cross-gap conduction, while the electron plasma frequency (ω_{pe}) limits electric field penetration in electrode plasmas. The CHICAGO PIC code includes algorithms that enable time steps to exceed the standard limits $\omega_c \Delta t \leq 1$ and $\omega_{pe} \Delta t \leq 1$, reducing run times by factors of 2 to 10. The governing equations are published in Refs. [22] and [72], so their importance is briefly illustrated in Sec. 4.1.

Prior to resolving the motion of relativistic particles and plasmas, they must be created in the vacuum. Methods for beam injection and space-charge-limited (SCL) [37] surface emission have been successfully applied to lower-energy accelerators [27, 11, 54, 52]. An additional requirement for *Z* simulations is modeling the desorption of electrode contaminants that form the surface plasmas. The CHICAGO algorithms developed for surface plasmas include more realistic surface physics and a fast, approximate plasma formation. These are used in Refs. [4], [5], [53], [71], and [72], and briefly described in Sec. 4.2.

The imploding *z*-pinch load impacts the current loss by increasing the inductance and, therefore, the electric field. This physics is discussed in Sec. 5. The change in inductance was originally modeled using a BERTHA [26] circuit at the load [5, 75], but a more realistic technique has been developed using a moving quasi-fluid liner [65].

Understanding the plasma environment of the diagnostics on *Z* has been a long-standing issue. In addition to describing *Z*'s electron environment in Sec. 5, we have implemented a technique for generating synthetic images in the visible for comparison to gated imaging diagnostics. This is described in Sec. 4.3.

4.1. Fast electromagnetic field solution

One of the unique advances in CHICAGO that enable multi-MA power-flow simulations is the fast "magnetic implicit" electromagnetic field solver [22, 72] that relaxes the time step constraint imposed by the electron cyclotron motion. The governing equations are laid out in Refs. [22], [71], and [72]. The impact of this algorithm is illustrated in Fig. 4-1, which compares the magnetic implicit and standard Boris [8] particle advances. Simulations of drifting electrons were constructed using static fields of $B_y = 1.2$ MG and $E_x = 18$ MV/cm with an $\mathbf{E} \times \mathbf{B}$ drift velocity of $v_{\text{drift}} = 0.05c$, which gives a Larmor radius of $r_L = 7.1 \times 10^{-5}$ cm. In both solutions, the cyclotron frequency is under-resolved by $\omega_c \Delta t = 13$, but only the magnetic implicit retains the correct v_{drift} and mean sheath width. In the standard Boris push, the electron trajectories exceed the required r_L by an order of magnitude.

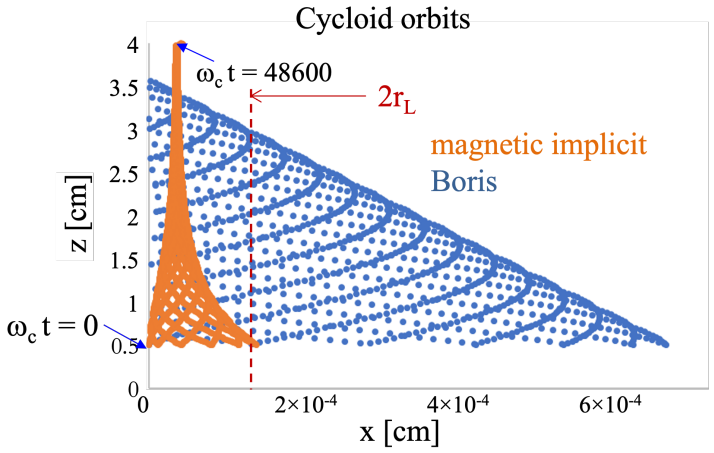

Figure 4-1 Electron trajectories from two electrostatic simulations of drifting electrons: the magnetic-implicit is shown in orange and the Boris particle push is shown in blue. The magnetic implicit better represents an $\mathbf{E} \times \mathbf{B}$ drifting electron in a MITL sheath.

Additional algorithms that improve code performance for larger time steps and cell sizes are an energy-conserving cloud-in-cell model to minimize electromagnetic fluctuations from individual macro-particles [7] and a time-biasing algorithm [23] to control the growth of electromagnetic fluctuations on the grid. An adaptive particle management algorithm was also developed for CHICAGO [73]. This may be used to limit the number of particles per species per cell, when the calculation can preserve the charge, energy, and momentum distributions.

4.2. Modeling electrode plasmas

The dominant mechanism for current loss on Z begins with the formation of electrode surface plasmas [56, 53, 24, 48, 71, 4, 5]. In simulations, SCL emission of electrons and ions contributes a few 10^5 A [56, 55, 4] but can not account for losses exceeding a MA that are routinely measured.

In the simulations presented in Sec. 5, SCL emission of electrons and protons is still included to capture their impact early in the pulse. Electron emission from the cathode is electric-field-induced, initiating after the local field exceeds the tolerance of the conductor [37], where 240 kV/cm [53] is used here for stainless steel. Protons are emitted from the anode after the local surface temperature increases by 400°C [58, 17]. The charged-particle emission becomes negligible when plasma formation is also modeled because the dense surface plasmas alter the electric fields adjacent to the electrodes.

Electrode plasmas are initiated as neutral surface contaminants (H_2O) thermally desorbed from both electrodes (on a cell-by-cell basis). The Arrhenius equation calculates the desorption rate as a function of the cell's temperature and remaining density of adsorbed contaminants ($n(t)$):

$$\frac{dn(t)}{dt} = -\nu_{th} n(t)\ e^{-E'(n)/(k_B T(t))}, \tag{2}$$

where $\nu_{th} \sim 10^{13}$ s^{-1}, $E'(n)$ is the effective binding energy, and T is the local surface temperature [51, 16]. The initial contaminant inventory on the electrode surfaces, $n(0)$, is 8.3 ML unless specified in tests of contaminant inventory. The Temkin isotherm computes $E'(n)$ via

$$E'(n) = E_d(1 - \alpha \frac{n(t)}{n_{ML}}) \quad [\text{eV}], \tag{3}$$

where E_d is the binding energy at infinitesimal coverage, α is determined experimentally. For the values used, $E_d = 0.8$ eV is consistent with molecular dynamics calculations and $\alpha = 0.17$ [4, 29].

The simulations presented here use a reduced model of plasma formation in which the desorbed neutrals are fully ionized within three grid cells from the surface. In this process, the H_2O molecule is fragmented and subsequently ionized according to $H_2O \rightarrow 2H^+ + O^+ + 3e$. This simplified model closely approximates distributions generated using detailed, Monte-Carlo ionization [3], but is much less computationally expensive.

To calculate the temperature for Eq. 2, the electrode surfaces are continuously updated for local Joule heating and particle energy deposition. The Joule heating model derives from [33]

$$T_J(t) = \frac{1}{c_v} \int_0^t \frac{j^2(t)}{\sigma} dt,$$

where σ and c_v are the conductivity and specific heat of the electrode (assumed constant). Assuming a linearly rising $j(t)$, the local temperature increase is [33]

$$\Delta T_J(t) \approx \frac{\vartheta \mu_0 H^2(t)}{2c_v}. \tag{4}$$

The surface energy factor $\vartheta = 1.273$ (from Table 5.2-II of Ref. [33]). This model is being replaced with a new CHICAGO surface treatment that calculates T_j without approximating $j(t)$.

Particle energy deposition (dE/dx) is calculated using the Bethe-Bloch equations for electron and ion energy loss [39]. The temperature increase ($T_d(t)$) per macroparticle is

$$\Delta T_d = \frac{dE}{dx} \frac{q}{ec_v A}, \tag{5}$$

where q is the macroparticle charge, e is the electron charge, and A is the cell's surface area.

4.3. Synthetic plasma imaging

A new capability for generating synthetic optical images has been developed using CHICAGO output and Spect3D from Prism[41]. This provides a direct comparison to experimental imaging diagnostics and aids in model and code validation.

The principal difficulty in connecting CHICAGO and Spect3D was the input/output formats that each software produced or accepted as an input. CHICAGO outputs in the binary format `.p4` while Spect3D expects input in a particular implementation in the binary format `Exodus II` format. That connection was made via a Python library to read in CHICAGO output, then output text files suitable for further processing by an auxiliary `C++` software, also provided by Prism.

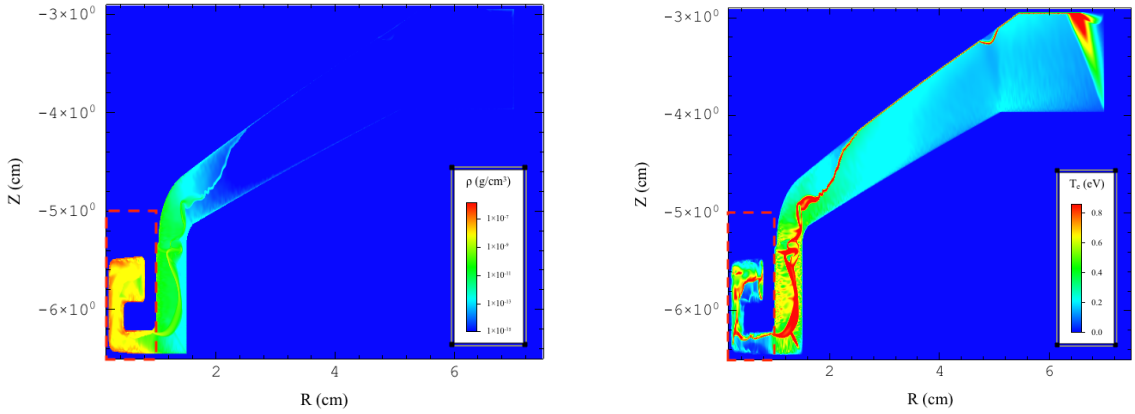

Figure 4-2 The plasma density (left) and temperature (right) from a CHICAGO simulation of the Power Flow Scaling geometry. The CHICAGO output is used to generate a synthetic image of the region outlined in the dashed red line. This is the region plotted in Fig. 4-3.

An example image is created for the Power Flow Scaling geometry, simulated in 2D cylindrical (r,z) coordinates. The simulated plasma density and temperature contours are shown in Fig. 4-2. These are the necessary input physical quantities for Spect3D. Only the portion bounded by the red dashed line in Fig. 4-2 is used to generate the synthetic image shown in Fig. 4-3. The image is not identical to either the temperature or the density from Fig. 4-2; rather, it is a convolution of both. Note that the synthetic image is actually a revolution of the red dashed region about the axis of symmetry. The image generation also takes into account the optical spectrum of the constituent elements of the plasma, in our case Oxygen (O^+), as shown in Fig. 4-4.

4.4. Shot modeling technique

Simulations of the hardware presented in Sec. 3 are conducted in 2D and 3D using the algorithms described in Secs. 4.1 and 4.2. 2D (r,z) simulations are used for high-resolution studies ($\Delta r,z = 20-40$ μm) of particle transport in the azimuthally-symmetric inner MITL. The cell

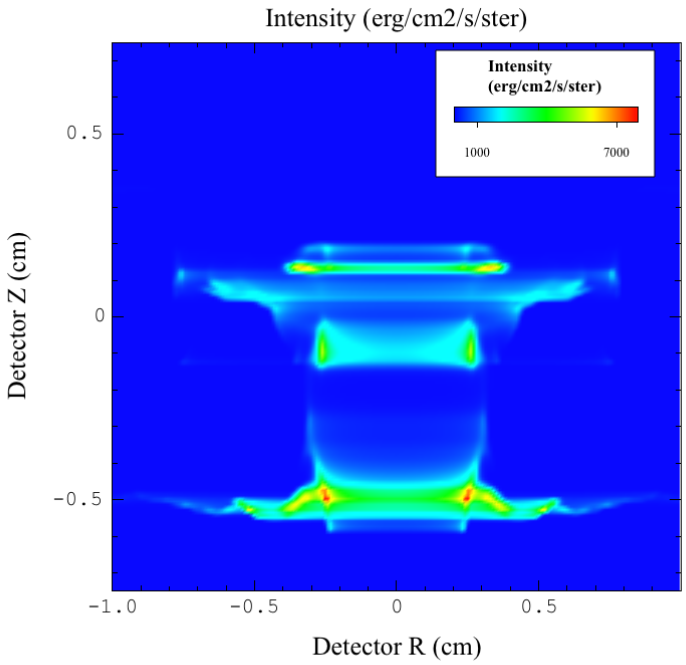

Figure 4-3 Spect3D synthetic image generated from the input data in Fig. 4-2.

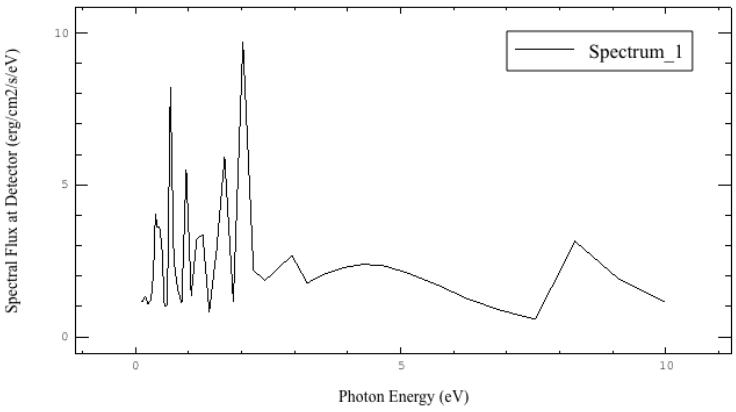

Figure 4-4 Spectrum of Oxygen (O^+) contributing to the synthetic image in Fig. 4-3.

sizes resolve the plasma dynamics for densities below 10^{19} cm^{-3} [6] that are typical of this region. Particle currents derived from 3D convolute simulations are injected at the outer boundary to emulate power flow exiting the convolute.

The convolute is modeled in 3D (r, θ, z) with symmetry boundaries and 100 μm minimum cell size. This grid size resolves the dynamics in plasma densities less than 10^{17} cm^{-3} [35]. This is

sufficient for the 10^{14} cm^{-3} peak densities in the convolute but not for densities near the load. The simulation geometries for the two main *Z* convolutes is shown in Fig. 4-5. They include the final 8 cm of the outer MITLs, the convolute, the inner MITL, and load region.

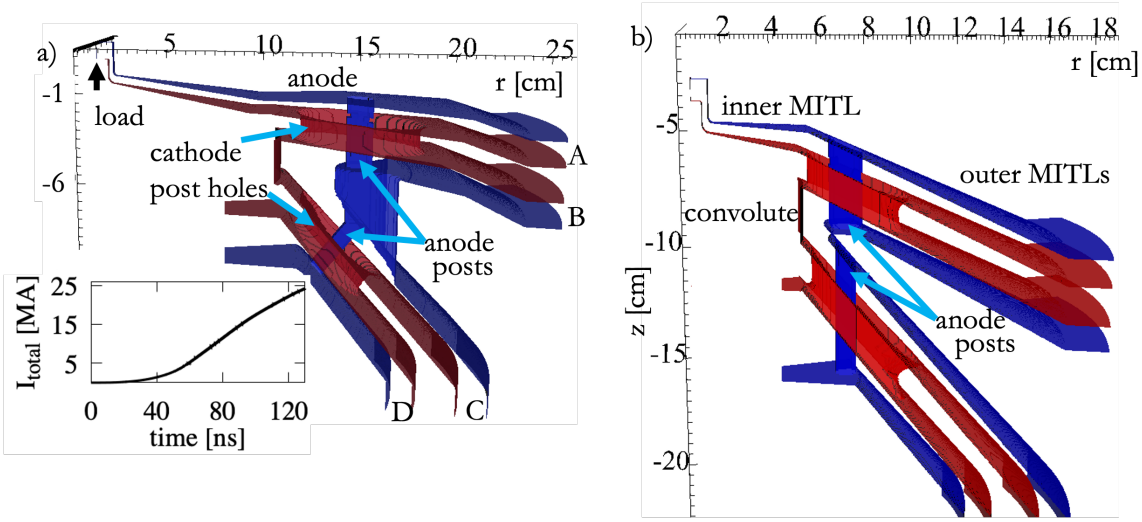

Figure 4-5 Illustration of the outer MITLs, double post-hole convolute, and inner MITL fielded for a) a ∅31cm convolute and b) a ∅15cm convolute. A pulse-generating circuit is attached at the four outer MITL feeds labeled A, B, C, and D. The total current is inlaid in a).

The circuit model components of Ref. [29] provide a realistic *Z* driving pulse. Four voltage pulses are supplied to a BERTHA [26] circuit originating at the the water convolute, just outside the insulator stack. In 3D models, the circuit is connected at four grid boundaries. In 2D, it connects to the outer radial boundary.

Two particle treatments are available in CHICAGO and both are used here. A kinetic particle treatment described in Refs. [71] and [4] is slower due to the large number of particles ($>$ 60 million) but more accurately follows particle evolution without approximations. A new fast fluid technique described in Ref. [72], assumes Maxwell distributions and an Eulerian remap to limit particles to one, maximum, per species per cell.

5. POWER FLOW ANALYSIS

The data presented in Sec. 3 are snapshots of small regions (SVS, chordal PDV, current probes) that are impacted by the cumulative physical processes in the entire system. Simulations were conducted of these shots to fill in the details in a self-consistent way - a way that simultaneously explains the low measured densities and the persistent current loss. The simulation geometries in Figs. 5-1 through 5-5 represent the hardware in Sec. 3 modeled using the techniques described in Sec. 4.4. Figures 5-3 and 5-4b use a new quasi-fluid liner model that is described in Ref. [65].

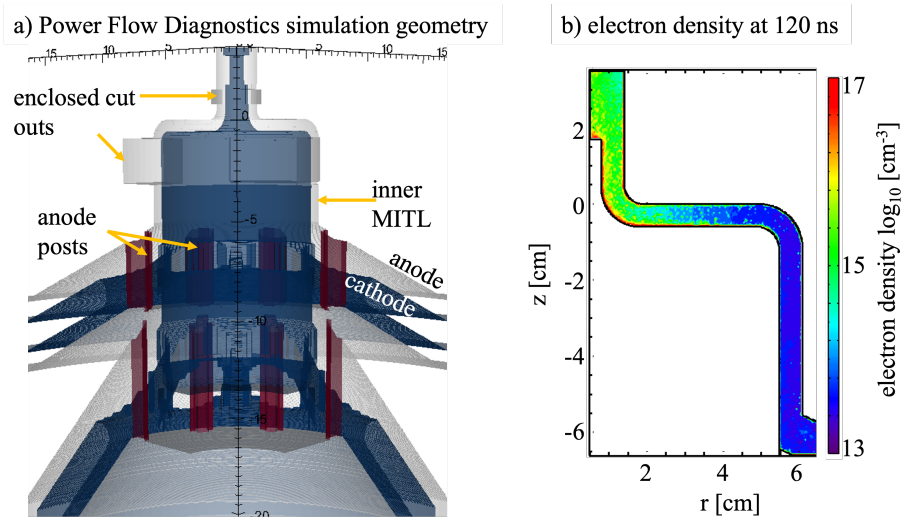

Figure 5-1 a) 3D CHICAGO rendering of Power Flow Diagnostics. b) electron density in the inner MITL.

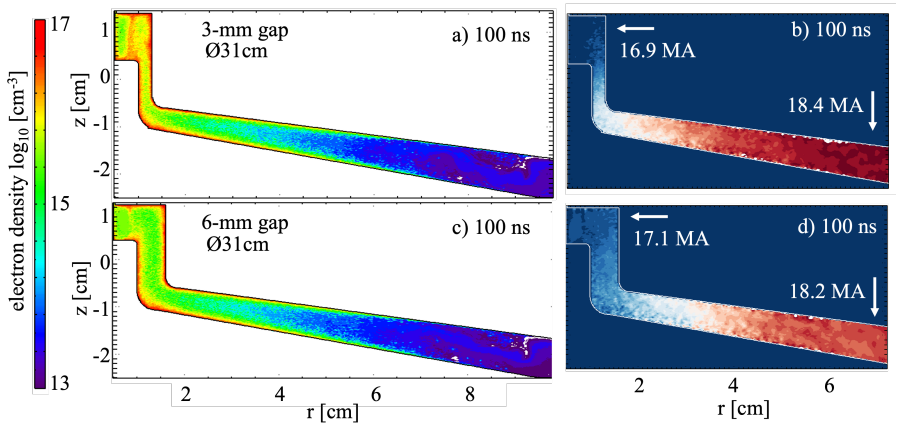

Figure 5-2 The 2D simulated Power Flow 18a electron density contours (left) and net currents (right) at 100 ns into the current pulse plotted in Fig. 4-5a. The densities are plotted on a log scale from 10^{13} to 10^{17} cm^{-3}. The current scales are linear, with the maxima and minima labeled at the outer radius and load, respectively.

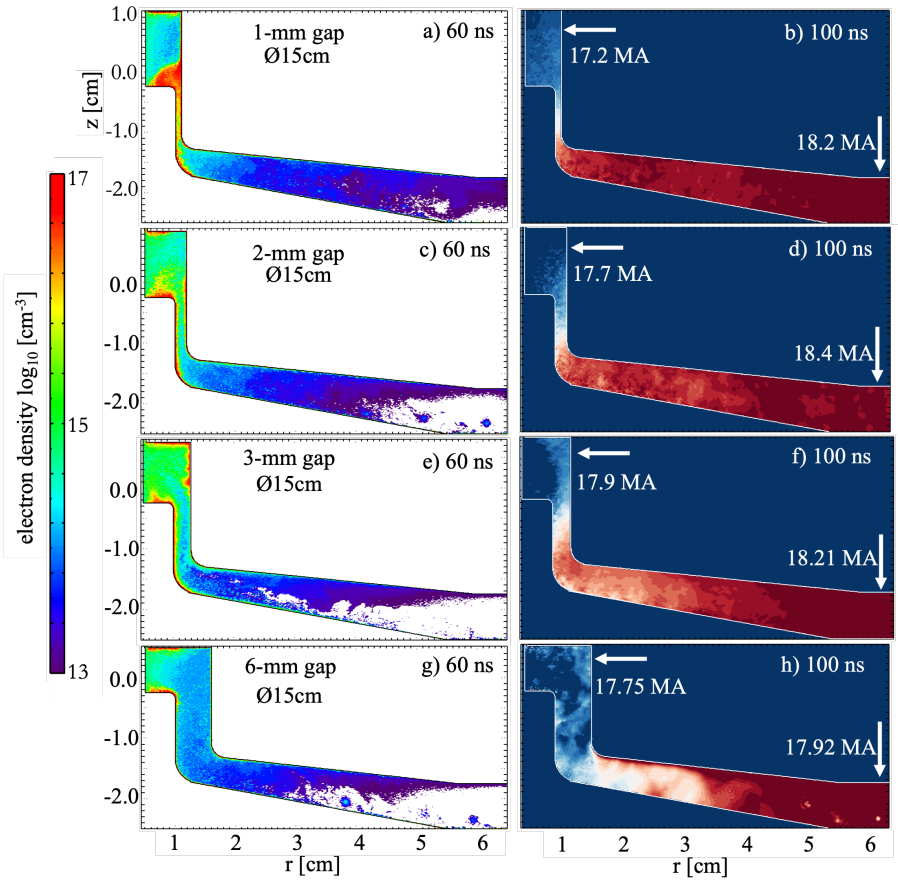

Figure 5-3 The simulated Power Flow Validation electron density contours (left) and net currents (right) in 2D. The 1 though 6-mm AK gaps (top to bottom rows)correspond to the hardware in Fig. 3-7. The densities are plotted on a log scale from 10^{13} to 10^{17} cm^{-3} midway through the pulse. The current snapshots are later and on linear scales.

Common behavior is noted in each simulation. The plasma generated on the electrode surfaces $\mathbf{E} \times \mathbf{B}$ drifts downstream, filling the AK gap and accumulating near the load. The variations in surface density gradients in Figs. 5-2, 5-3, and 5-4 result from this flow and from associated Kelvin-Helmholtz instabilities. In each case, there is no current loss in the inner MITL prior to the plasma build-up. Uninsulated SCL emission leads to early, transient losses in the convolute of $500 - 800$ kA (for the 15-cm and 31-cm-diameter, respectively) but higher losses occur only after surface plasmas are observed.

The currents plotted in Figs. 5-2 through 5-5 show loss occurs over a volume that is related to, but not 100% coincident with, plasma density. This is the Hall-related loss mechanism that is described in Sec. 5.4. The Hall mechanism is related to inductance as discussed in Sec. 5.3. Gap closure and MITL bends are also discussed, but as shown in the data in Sec. 3, they are not implicated in current loss. After a couple of shot series seeking the enhanced ion current mechanism, it is also not implicated in the inner MITL.

Additional simulations and their comparisons to data are presented in the next section to provide

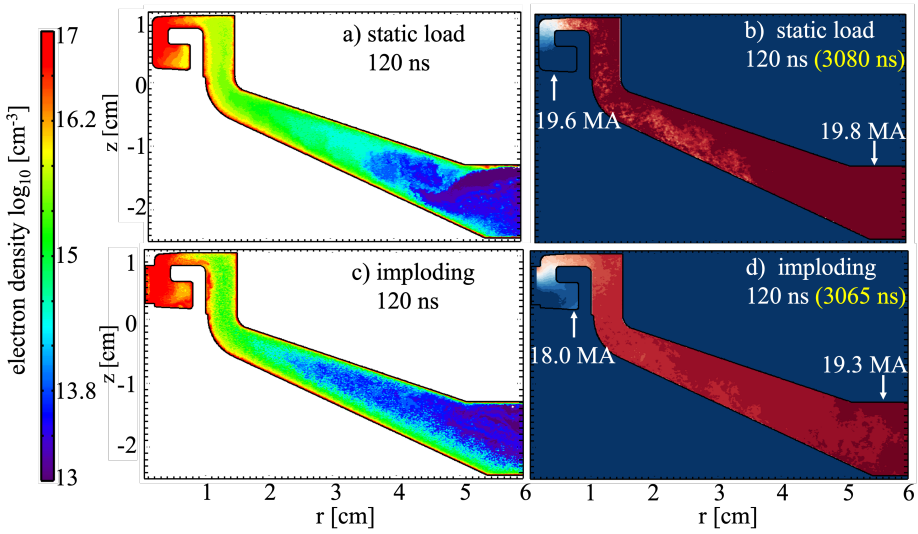

Figure 5-4 The simulated Power Flow Scaling electron densities (left) and net currents (right) in 2D. The density contours for a) the static and b) the imploding loads are plotted on a log scale from 10^{13} to 10^{17} cm^{-3}. The current values at the outer radius and load are labeled in b) and d). The snapshots are near peak current (120 ns). The corresponding Z machine times are noted in yellow for comparison to Fig. 3-13.

confidence that Figs. 5-1 through 5-5 capture the relevant physics. A discussion of the current-loss theories under test follows.

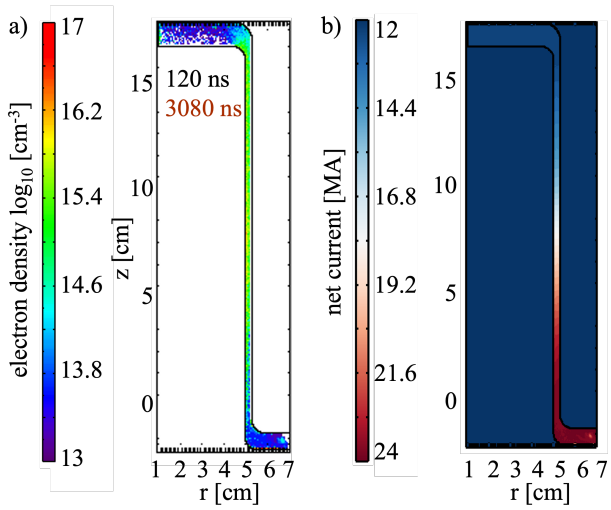

Figure 5-5 The simulated Reverted Convolute a) electron density and b) net current in the inner MITL.

5.1. Code validation

The CHICAGO code is validated against measured load currents, which are a comprehensive diagnostic. They are impacted by unmagnetized current losses in the convolute, time-dependent plasma formation and related losses in the convolute and inner MITL, and changes in load inductance. The simulated losses in Power Flow 18a, Power Flow Validation, and Power Flow Scaling, shown graphically in Figs. 5-2 through 5-4, all agree with data. This is demonstrated in Fig. 5-6 for Power Flow 18a.

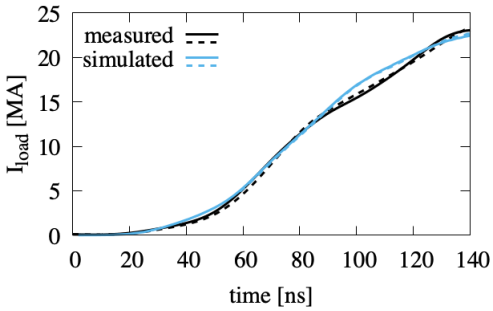

Figure 5-6 The simulated and measured load currents for Power Flow 18a (Fig. 13 from Ref. [4]). Compare to net currents plotted in Fig. 5-2.

The Power Flow shot hardware is typically in the 5 nH range for inductance. The MagLIF concept provides an example of current loss in a higher-inductance (6.9 nH) system. Simulations are compared to data for two applied magnetic field strengths, 0 T and 15 T. The net current contours at 120 ns are plotted in Figs. 5-7a and b for 0 T. The currents are compared in Fig. 5-7c. Differences in the applied magnetic field may alter particle trajectories in the inner MITL and delay heating in some locations, but plasma densities in the transmission line eventually exceed 10^{16} cm^{-3} and losses at peak power are similar.

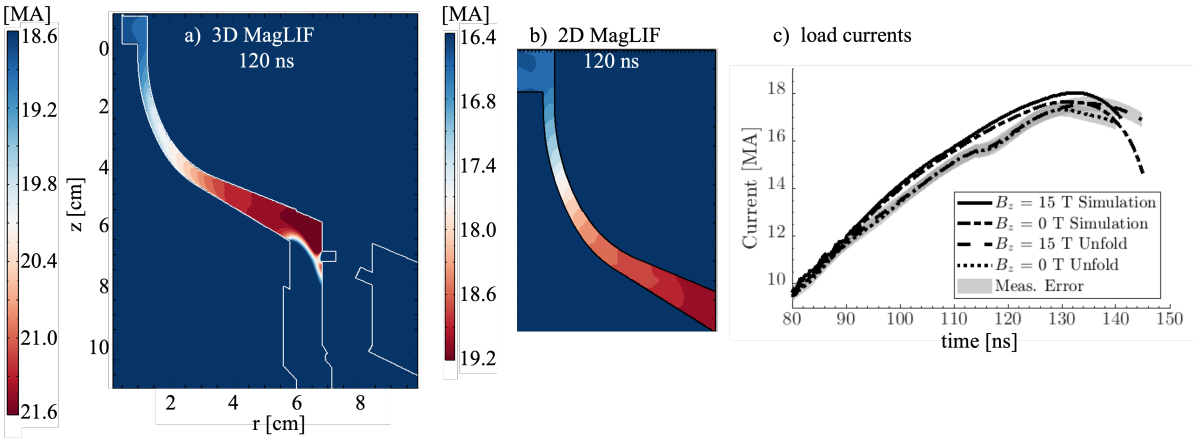

Figure 5-7 The net current contours in a) 3D and b) 2D CHICAGO multi-fluid simulations of MagLIF. c) (Figure 10 from Ref. [75]) Load currents from simulations and data with and without a 15 T applied B_z.

A comparison of line and load current for a low-inductance (2.9 nH) system is shown in Fig. 5-8.

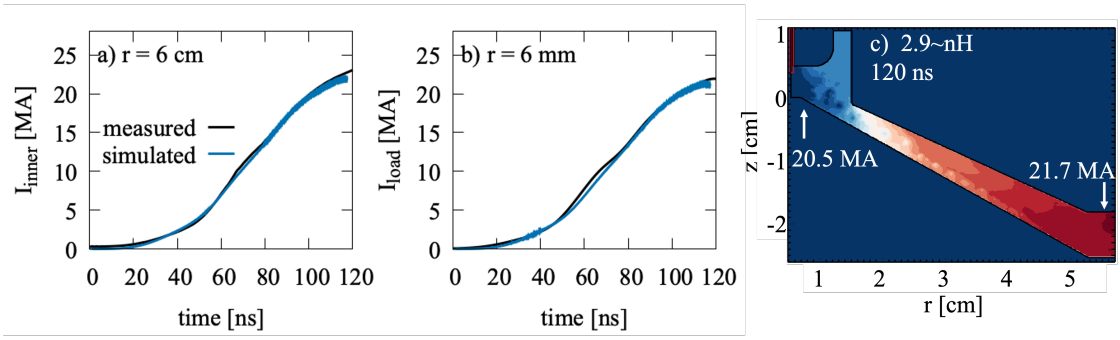

Figure 5-8 Total current delivered to the a) inner MITL ($r = 6$ cm) and b) load ($r = 6$ mm) for a 2.9 nH inner MITL. Measurement is shown in black and simulation in blue. c) The net current contour at 120 ns.

Code validation for changes to the outer MITLs as well as the inner MITL is provided by the MagLIF metallic coatings shots fielded with debris shields in the four outer MITLs. The electron density contours at 120 ns are plotted in Figs. 5-9a and b. The currents are compared in Fig. 5-9c.

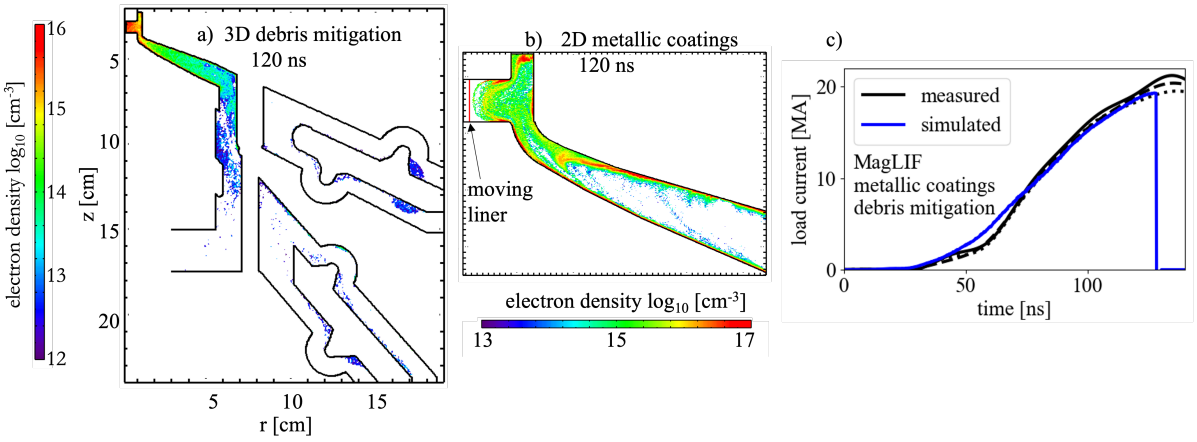

Figure 5-9 The density contours in a) 3D and b) 2D CHICAGO multi-fluid simulations of MagLIF metallic coatings with debris shields. c) Load currents from simulations and data.

5.2. Enhanced ion current

In the enhanced ion current theory for current loss [29, 68, 55], electrons dominate the current entering the inner MITL from the convolute. Their negative space-charge enables more SCL emission of positive ions, leading to positive-ion-dominated loss currents. This assumes ions are able to cross the AK gap in the presence of powerful ($>$ 100 T) magnetic fields.

To estimate when and where ions are able to cross the AK gap, we calculate the MITL radius below which the ions are magnetically insulated. We use the current pulse in Fig. 4-5a to calculate the azimuthal magnetic field ($B_\theta(r,t)$) and the voltage ($V(t)$) at $r = 5$ cm to estimate the non-relativistic ion velocity. From these, an ion is insulated when its Larmor radius equals the gap width ($r_L = d$), which occurs out to the MITL radial position

$$r_{max} = \frac{e}{m}\frac{\mu_0 I(t)}{2\pi}\left(\frac{m}{2ZeV(t)}\right)^{1/2} d. \tag{6}$$

This is plotted in Fig. 5-10 for H^+ and O^+ for 7-mm and 3-mm gaps.

A 7-mm AK gap at the entrance to the inner MITL is a more typical geometry, but it shows that H^+ are emitted already insulated and can not cross the gap. O^+ are not insulated but their contribution to a SCL current is reduced by their mass according to the non-relativistic SCL current density [37]:

$$j_{CL} = \frac{4\varepsilon_0}{9}\left(\frac{2Ze}{m}\right)^{1/2}\frac{V_0^{3/2}}{d^2}, \tag{7}$$

where V_0 is the voltage drop, d is the AK gap width, m is the particle mass, and Z is its charge state.

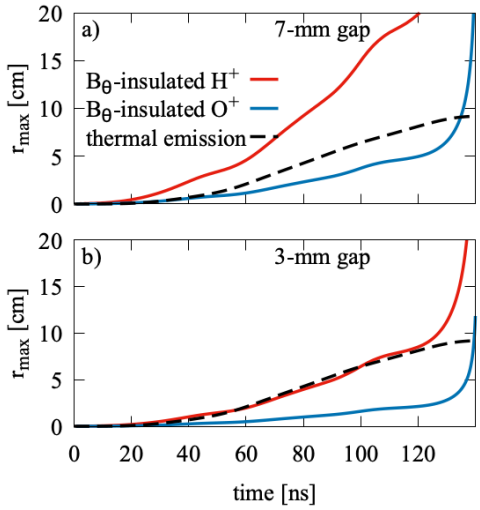

Figure 5-10 The maximum radius at which ions are magnetically insulated as a function of time (Eq. 6) for a) a 7-mm AK gap and b) a 3-mm gap. The H^+ and O^+ ions are plotted in red and blue, respectively. The maximum radius for thermal emission from Eq. 4 for $\Delta T = 400$ K (in black).

For the 3-mm gap (Fig. 5-10b), H^+ may be slightly above the threshold for insulation and detection using Faraday cups. This was the gap was chosen for the Inverted and Reverted Convolute shots (Sec. 3.5). The theoretical prediction for enhanced ion current loss for the Reverted Convolute peaks at 2.5 to 2.8 kA/cm^2 (1.2 to 1.4 MA) at 82.5 ns and reduces to 0.5 to 1 kA/cm^2 (0.25 to 0.5 MA) at 100 ns [67]. The measured densities in the Faraday cups are below this prediction, at 0.2 to 0.5 kA/cm^2 and falling to zero at 90 ns. This results makes a generous assumption that the MITL illumination did not impact this probe. This result does not support the measured current loss plotted in Fig. 3-15, which increases to $\gtrsim$ 4 MA at 100 ns.

Neither the Inverted nor the Reverted Convolute shots support an enhanced ion current loss in the inner MITL on *Z*. The Reverted Convolute currents counter these theoretical predictions. This loss mechanism has not yet been explored for the convolute region, where bipolar currents (counter-streaming electrons and ions) may contribute to losses.

5.3. Gap closure, inductance, and MITL bends

Electrode plasmas occur in every *Z* shot. Therefore, all of the shots detailed in Sec. 3 provide information on plasma formation and particle transport. Additionally, the Power Flow 18a, Power Flow Validation, and Power Flow Scaling platforms (Secs. 3.2 through 3.4) were designed with varying AK gaps, fixed inductances, and 90-degree bends in the transmission lines to test the impact of those structures on current loss. The combined analysis of these shots and accompanying simulations, presented here, provides a consistent picture of plasma dynamics in power flow.

The simulated plasma dynamics are usually verified indirectly from MITL and load current probes, but are more directly measured in the Power Flow Diagnostics shots. Its simulated electron density map is shown in Fig. 5-1b. From this model, line-outs at $z = 1$ cm taken at three times during the pulse rise are plotted in Fig. 5-11. The density distribution across the AK gap is seen to peak near the electrodes, dropping 1 to 2 orders of magnitude within 200 μm from the surfaces. These gradients reduce during the pulse as the contaminant inventory is depleted and the surface plasmas are transported in to the gap.

The data in Figs. 3-4 and 3-5 are consistent with this description. The measured plasma densities are below 10^{15} cm^3 until 3100 ns in Fig. 3-5, 125 ns into the pulse and 25 ns after peak current. The measured and simulated densities in the gap at similar currents are $\sim 10^{16}$ cm^{-3}. This suggests the surface plasmas experience some magnetic confinement, as predicted [5], and that the contaminant inventory is near 2 to 8 ML. More can not be said about the contaminant inventory because plasma is continuously transported downstream during the pulse and the inductive electric field reverses sign after peak current reversing the drift direction. The late-time plasma redistribution complicates discussions of the contaminant inventory and plasma expansion velocity.

This picture of high ($> 10^{17}$ cm^{-3}) surface densities that are delayed in filling the AK gap due to the magnetic field is confirmed in the gap-closure tests in Power Flow Scaling (Fig. 5-4) and Power Flow Validation (Fig. 5-3). There was an expectation that AK gaps of 2-mm and less experience plasma gap closure [64], but the shot currents, Figs. 3-13 and 3-8, counter this. The

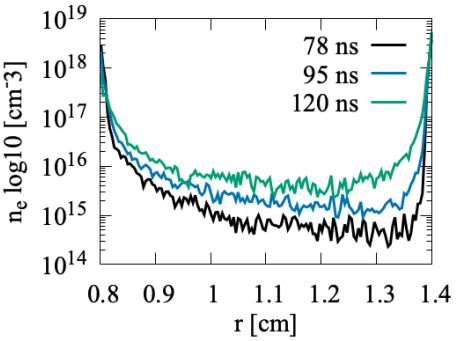

Figure 5-11 Simulated electron density in $8 \leq r \leq 14$ mm for Power Flow Diagnostics.

simulations in Figs. 5-2 to 5-4 show the surface densities remain near 10^{17} cm^{-3} (see data in Fig. 3-9), particularly at small radius, while the density transported into the AK gap is down by 2 orders of magnitude. The plasmas do not expand orthogonally away from the electrodes but $\mathbf{E} \times \mathbf{B}$ drift downstream. The current is lost over a volume in which plasma is accumulating and in which the electric field is non-zero.

The next section describes how current loss is a function of local electric field via the Hall-loss mechanism. This explains the long-noted correlation between load inductance and current loss. Higher initial inductances, or increases in inductance as the load implodes, drive higher inductive electric fields. The uptick in current loss during a liner implosion is seen in Fig. 5-4d.

A 90-degree bend in a MITL is generally not an impediment to a drifting plasma. To test this, a conical MITL was designed with the same inductance (3.44 nH) and imploding load as the Power Flow Validation series. The delivered currents are were consistent with this series, as shown in Fig. 3-8a. For further confirmation, the Power Flow Scaling geometries in Figs. 3-12 and 5-4 also have 90-degree bends into a 2-mm AK gap and these shots are essentially lossless (see Fig. 3-13) [45]. The simulated currents in Figs. 5-4b and 5-4d-h agree with these low losses.

5.4. Hall-conductivity-related current

The current loss mechanism at work on *Z* appears as a parallel load (rather than a complete short), manifests near 15 MA for a typical load (see Figs.3-8 and 3-15), and increases with the load inductance. The gap-closure mechanism is not adequate because it would ultimately short transmission lines with small gaps for a thermal expansion velocity. Current loss via $> 10^{18}$ cm^{-3} plasma streamers would also short the transmission line. This is the density regime of gas-puff *z*-pinch loads [13, 30], which consistently ionize, conduct the full load current, and implode on axis via the $\mathbf{j} \times \mathbf{B}$ force.

The kinetic power-flow simulations in this report demonstrate current loss without high-density gap-closing plasmas and streamers. Instead, low-density ($10^{15} - 10^{16}$ cm^{-3}) plasmas appear to conduct current in volumes that are cm's long. This can not be attributed to the standard conductivity which is much too small. In the direction transverse to the magnetic field, the

conductivity ($\sigma_\perp$) is reduced from the parallel, or unmagnetized, conductivity (σ) by $(1+\omega_c^2/\nu_c^2)^{-1}$ [9], where ω_c is the cyclotron frequency and ν_c is the particle collision rate. In the inner MITL of *Z*, the magnetic field exceeds 200 T but collision rates are low in the hot, low-density plasmas, so $\omega_c/\nu_c > 10^4$ and $\sigma_\perp$ is 8 orders of magnitude smaller than σ.

In this regime, the contributions from the off-diagonal elements of the conductivity tensor [1] become significant [70]. The tensor elements are defined in the generalized Ohm's law [10, 61]:

$$\mathbf{j} = \sigma \mathbf{E'}_{\parallel} + \sigma_\perp \mathbf{E'}_{\perp} + \sigma_H(\mathbf{b} \times \mathbf{E'}_{\perp}),$$

where $\mathbf{E'}$ is the effective electric field in the ion inertial frame, the tensor elements are

$$\begin{aligned} \sigma &= \frac{ne^2}{m\nu_c} \\ \sigma_\perp &= \frac{\sigma}{1+\frac{\omega_c^2}{\nu_c^2}} \quad \text{and,} \\ \sigma_\wedge = \sigma_H &= \sigma_\perp \frac{\omega_c}{\nu_c}. \end{aligned} \tag{8}$$

σ_H is the off-diagonal Hall conductivity that establishes a current perpendicular to $\mathbf{E'}$ and $\mathbf{B}$.

It should be noted that Eq. 8 is derived in a fluid description that assumes Maxwell distributions. Current loss via σ_H nonetheless fits the bill by scaling linearly with plasma density and electric field, and σ_H is only 4 orders of magnitude smaller than σ in the inner MITL.

To test this, a time-dependent, volume-averaged value of σ_H is calculated from Eq. 8 for each Power Flow Validation simulation in Fig. 5-3 using $\mathbf{B}(t)$, $n_e(t)$ and $\nu_c(t)$. A Hall-related current is calculated using $\sigma_H(t)E(t)A$, where A is the anode surface area in the loss region [5]. The simulated current loss ($I_{loss} = I_{outer} - I_{load}$) is compared to the Hall-related current in Fig. 5-12.

The simulated and theoretical currents in Fig. 5-12 agree well except at early times for the smaller gaps: Fig. 5-12c and d corresponding to the net currents in Figs.5-3b and d. In these two cases, a plasma density exceeding 10^{17} cm^{-3}, along a length of a few mm, carries most of the loss current. Local values of σ_H and Hall-related current are calculated and included as points in Fig. 5-12c and d, restoring agreement. The high current densities generate non-negligible $j \times B$ acceleration toward the load. While the denser plasma is clearing, the plasma density is still increasing in the larger inner MITL volume, so the loss current fluctuates without dropping to zero.

The simulation/theory comparison was also conducted for Power Flow 18a (Fig. 15 in Ref. [5]) and each simulation/data comparison in Sec. 5.1 is an indirect comparison. However, the circuit model is frequently used to predict shot performance and also compares well to most measured currents. The most unambiguous test of the simulation-derived Hall-loss theory is found on the Reverted Convolute platform, which was designed to increase the losses to large values. Current loss predictions were made for an enhanced ion current (Sec. 5.2), for gap closure via the circuit model, and from the simulation in Fig. 5-5. We noted that the enhanced ion current predicted 0.5 MA of loss at 100 ns. The circuit model predicted no losses. The simulation predicted 4 MA of loss at 100 ns, increasing with time, as shown in Fig. 5-13a for the assumed 8.3 ML contaminant inventory. The simulations are shifted -2960 ns from *Z* machine time in Fig. 3-15.

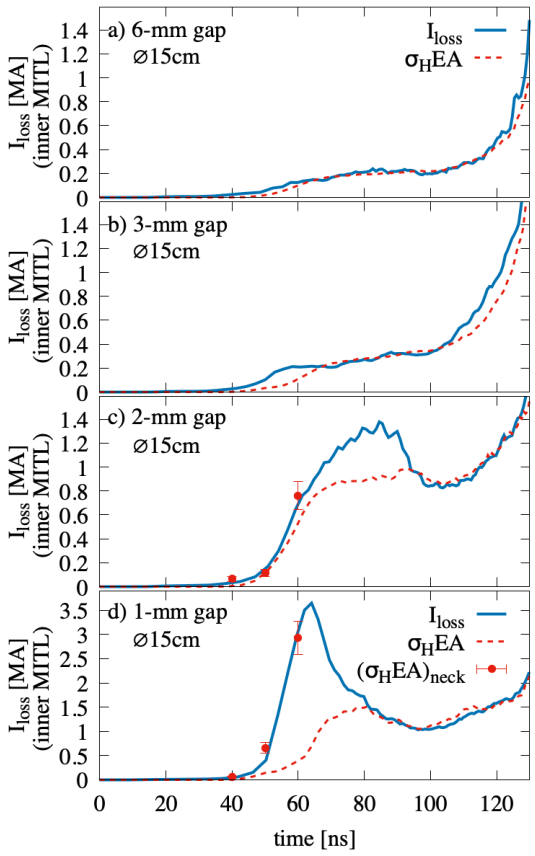

Figure 5-12 Current loss compared to an estimate of the Hall-related current ($\sigma_H EA$) for Power Flow Validation (Fig. 5-3). The points in c) and d) are calculated from local values in the minimum AK gap region. This is Fig.14 from Ref. [5].

The measured current loss at 100 ns is $\sim$ 4.5 MA, if the PDV is used instead of the final IDTL. This is consistent with Fig. 5-13a. However, the loss rate slows in data relative to the prediction, so additional simulations were run assuming 1, 2, 4, and 6 ML. The growth in current loss does slow when the contaminant inventory is reduced, as shown in Fig. 5-13b. The simulations at 1 to 2 ML provide the best agreement with data.

The Reverted Convolute platform appears more sensitive to the amount of electrode contaminants than others modeled. Its 10-cm-diameter coaxial transmission line heats more slowly than standard inner MITLs. This makes it more sensitive to the desorption rate in Eq. 2, which, for the rapid temperature increases in most inner MITLs, typically acts as a switch to ν_{th}.

6. KEY PHYSICS IN ELECTRODE PLASMA FORMATION AND CURRENT LOSS

Thermally-generated electrode plasmas drive current loss on Z. Simulations that do not include plasma formation do not reproduce the measured losses [47, 56, 57, 42, 55]. Diagnostics

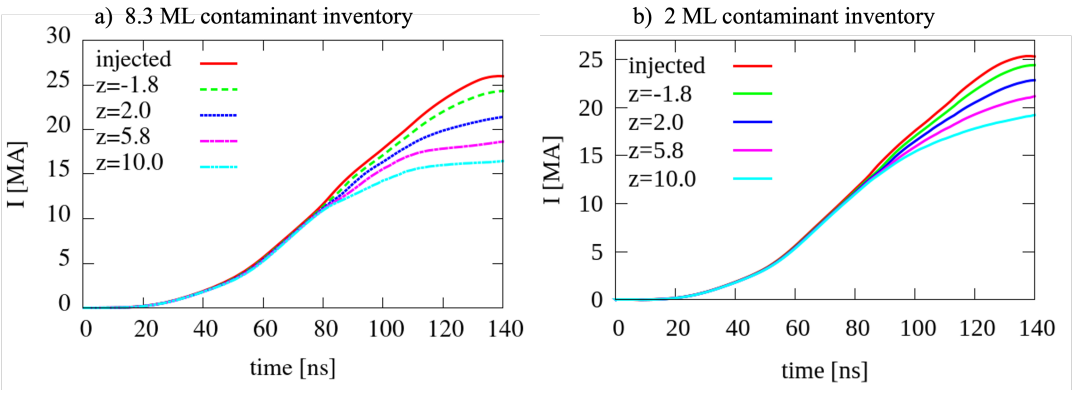

Figure 5-13 The simulated Reverted Convolute currents as a function of position assuming a) 8.3 ML of contaminants and b) 2 ML. The labels denote the positions in Figs. 3-14 and 5-5.

consistently record plasma coincident with current loss [48, 49]. While uninsulated current sheaths lead to early, transient losses in the convolute of 500 – 800 kA (for the 15-cm and 31-cm-diameter, respectively), convolute losses greater than a MA occur only after surface plasmas form (see Fig. 10 of Ref. [4]). In the inner MITL, ions and electrons are insulated upon emission (see Eq. 6 and Fig. 5-10).

We note that "thermally-generated" plasma is distinguished from the tenuous cathode plasma generated during SCL electron emission. SCL emission treats the electrodes as infinite sources of electrons that respond to the local electric field, with no regard to the work function of the electrode metal. It has long been held that SCL electrons are sourced from a low-density plasma in contact with the metal [50]. Cathodes are not cold in this regime, though not traditionally Joule heated (Eq. 4). Only a small fraction of a ML is required to support this current.

For transmission lines operating above 10^5 A/cm, Joule heating and particle energy deposition (Eqs. 4 and 5) increase surface temperatures into a range where contaminant desorption (Eq. 2) becomes significant. Multiple ML may be liberated in tens of ns [3, 40]. This is illustrated in Fig. 6-1 which shows the desorption rate during a Z pulse calculated from Eqs. 2 and 3, normalized by $1/n$ and using only Joule heating (Eq. 4). The full inventory is rapidly converted into a surface plasma at a 1-cm radius. At 5 cm, the inventory is only fully desorbed by peak current.

Full contaminant desorption does not imply that the plasmas are expanding freely, or even uniformly, into the AK gap. Instead, the strong magnetic fields that heat the electrodes to emission also confine the charged particles near the surfaces. This confinement trifurcates the conductivity, as discussed in Sec. 5.4. It also leads to what may be considered two plasma distributions in the inner MITL: a colder, denser ($10^{17} - 10^{18}$ cm^{-3}) surface plasma and a hotter, lower-density ($10^{14} - 10^{16}$ cm^{-3}) plasma that was accelerated into the AK gap by the electric field. The density distributions are evident in Figs. 5-1 through 5-5 and magnified in Fig. 6-2a for the Power Flow Scaling geometry. The surface plasmas, particularly at the early time shown (60 ns), are three orders of magnitude denser than the gap plasma. Figure 6-2b shows four orders of magnitude separate the temperatures.

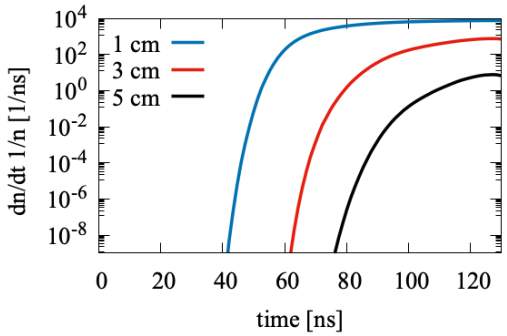

Figure 6-1 The normalized desorption rates from Eqs. 2 and 3 calculated from Joule heating (Eq. 4) at radii of 1, 3, and 5 cm.

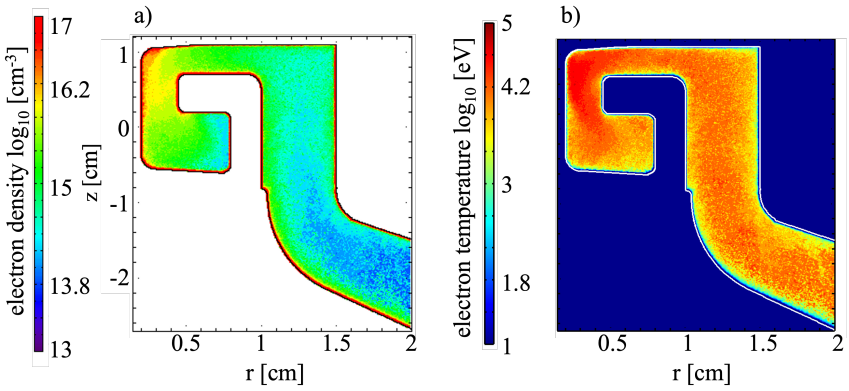

Figure 6-2 The simulated Power Flow Scaling electron a) densities and b) temperatures at 60 ns. Both contours are plotted on log scales.

The mechanism for transport into the gap is more fully explored in Ref. [3]. A breakdown model shows contaminants rapidly ionizing and forming a $10^{15} - 10^{18}$ cm^{-3} plasma that is effectively resistive while weakly collisional because it is created within, and rapidly penetrated by, the magnetic field. The surface plasma advects the cathode potential, in gap-closure fashion, but a simple plasma expansion is not obvious. Instead, the applied **E** field penetrates surface plasma a distance measured in skin depths and accelerates particles into the AK gap. Particle currents entering the inner MITL from the convolute assist in transporting plasma from the surface. By generating density and velocity gradients, they seed instabilities and turbulence [71]. The exact mechanisms are under investigation.

As plasma is transported into the AK gap, it will also $\mathbf{E} \times \mathbf{B}$ drift downstream. This is forms the graded density contours in Figs. 5-1 through 5-5. Plasma collects downstream, where the drift velocity, $v_{\text{drift}} = \mathbf{E} \times \mathbf{B}/B^2$, decreases. More plasma fills the gap downstream, contributing to current loss there.

The simulated cross-gap currents are well-approximated by the Hall current in the generalized Ohm's law, as detailed in Sec. 5.4. The Hall-related current, $\sigma_H(t)E(t)A$, increases with the local plasma density, electric field and surface area along which the plasma is accumulating. The latter are directly related to transmission line inductance, which explains the observed correlation. The

total amount of contaminants is proportional to the surface area, which increases with inductance, so the plasma density is also a function of inductance.

When a plasma begins to support large current densities, manifesting similar to an arc, the $\mathbf{j} \times \mathbf{B}$ force changes the density distribution. The denser plasma sweeps downstream and current is partially restored to the load. Like magnetic insulation, this plasma clearing mitigates current loss in pulsed power systems. The details of plasma clearing and its impact on the load are under investigation.

7. EXPERIMENTAL AND SIMULATION GAPS

While our understanding of electrode plasma formation and evolution has advanced significantly as a result of the power-flow studies reported here and in Refs. [5] and [3], important physics still needs to be explored. Significantly, current loss in the convolute is still not well understood, and this impacts the designs for current addition in the NGPP. Similarly, plasmas near the load are also not well understood. Plasma density measurements confirm dense surface plasmas (>10^{17} cm^{-3}) and lower-density gap plasmas ($10^{14} - 10^{16}$ cm^{-3}), more sensitive diagnostics are needed to characterize plasma species and velocities. New code development is also beginning to address this [66]. Power-flow plasmas entering the load region ($r \lesssim 8$ mm) may impact liner implosions and yields. Plasmas generated near the load have contributions from melt and vaporization, and these processes will occur earlier and over a larger surface area in the NGPP.

These gaps in our understanding will be addressed in planned shot series on *Z* and on Sandia's 1-MA Mykonos linear transformer driver [32, 54]. Hardware designs are pushing the electromagnetic field and plasma environments closer to NGPP conditions, diagnostics are being developed to more precisely measure plasma density [2, 25], and simulations are being conducted to characterize the plasma environment these diagnostics may expect. Some of these studies are briefly described here.

A shot series is underway that is dedicated to exploring current loss in the convolute and how it scales with peak current density. Data in this series will be analyzed against the 3D simulations of our present experimental campaign in Secs. 3 and 5. While some convolute results are reported in Refs. [24] and [4], our understanding of the convolute is not complete. The data from the Faraday cups fielded in the anode posts in Fig. 3-10 show charged particles in the convolute responding to losses in the inner MITL.

The Power Flow Scaling shot series will continue to push NGPP electromagnetic field conditions with smaller AK gaps than shown in Fig. 3-12 and more plasma and current diagnostics fielded at smaller radii. The interior inductance will be increased to match the electric field and current density of a 70-MA inner MITL.

The Power Flow Validation series shot with the 1-mm AK gap has measured current fluctuations, shown in Fig. 3-8b, which are similar to the simulated fluctuations in Fig. 5-12d but with ~ 4 MA more loss. This may be evidence of plasma clearing, in which streamers of higher-density plasma ($\geq 10^{18}$ cm^{-3}) form and are swept downstream by the $\mathbf{j} \times \mathbf{B}$ force. The dynamic materials experiments also show this phenomenon, and data from these shots will be compared to simulations to confirm the densities and timescales involved.

To that end, recent algorithm improvements in CHICAGO have enabled more numerically stable 3D simulations of the convolute and inner MITL. The code is also being compiled on higher performance compute platforms. This has enabled large-scale models of the dynamic materials experiments on *Z*, which have pulse lengths in excess of 1.4 μs. In addition to plasma clearing, these simulations will help understand what leads to variations in the long-pulse shapes and how slower heating impacts plasma evolution. The simulations may also reduce operating costs. Dynamic materials experiments typically require an allocation of pulse shaping shots prior to the

actual experiments. These could be obviated by simulation that predict the pulse shape for given Z machine voltages and timings paired with load inductances and current loss.

Any discrepancies in IDTL and PDV visar current measurements will be investigated with a proposed simulation technique for estimating particle energy deposition in PDV current probes. In this technique, kinetic particles generated in power flow will impact a solid-density, MHD-like plasma PDV visar flyer plate. The unique collision and energy deposition algorithms extend the boundaries of state-of-the-art hybrid fluid-PIC modeling. Simulations are also being conducted to characterize the plasma environment surrounding diagnostic apertures, such as used in fielding IDTLs.

Slightly away from the electrode surfaces, theory and simulation will address plasma instabilities that may increase transport into the AK gap. The evolving plasmas will be characterized using newly developed interferometry [25] and PDV diagnostics.

Finally, important work continues on methods to reduce the contaminant inventory on the electrode surfaces to arrest current loss. A plasma cleaning platform is being tested on Mykonos [36] that bombards electrodes with high energy particles to clean the surfaces and reduce contaminant plasma density.

8. CONCLUSION

A coordinated campaign of experiments, simulations, and theory has been undertaken over the last three years to advance our understanding of power flow physics in transmission lines operating above 20 MA. This multi-discipline effort has enabled us to progress from early speculation about plasma formation times, densities, and locations. The acquired knowledge is being used to increase the efficiency of Sandia's Z accelerator and to develop the NGPP facility.

These dedicated power-flow experiments, summarized in Table 1-1, used IDTL and PDV visar to measure load currents, SVS to measure surface plasma densities, chordal PDV to measure gap plasma densities, and Faraday cups to measure charged particle fluences. PIC simulations were conducted in support of each shot using realistic hardware and Z voltage pulses. The simulations of the challenging plasma environment of Z were enabled by hybrid kinetic/fluid algorithm developments.

The combined analysis of simulation and data confirms that electrode plasmas have the most detrimental impact on current delivery. Transmission lines with low measured densities ($< 10^{16}$ cm^{-3}) benefit from low losses. These low densities may occur even in transmission lines with constriction points (localized small gaps) if the drift velocity is sufficient to sweep the plasma farther downstream.

Experiments tested the theoretical current-loss mechanisms of enhanced ion current, plasma gap closure, and Hall-related current. These mechanisms are not mutually exclusive and may be coincident in the inner MITL and upstream in the convolute (current adder). The final-feed geometries tested here, however, confirm the dominance of a lower-density plasma that is more consistent with Hall-related current and not gap closure or streaming high-density plasma. Likewise, the presence of ions may create a bipolar current in the convolute, but neither the measured inner MITL currents nor the ion flux agree with the theoretical prediction of an enhanced ion current loss.

The picture of plasma formation and transport formed from experiment and simulation is informing hardware designs being fielded on Z now and being proposed for the NGPP facility. Beginning with the rising pulse on Z, the transmission lines experience increasing electric and magnetic fields, and therefore, increasing current densities and temperatures. While the magnetic field ($\mathbf{B}$) increases with decreasing radius, the electric field ($\mathbf{E}$) is a function of the local transmission line AK gap and proximity to the short-circuit or gas-breakdown load. Particle emission follows the progression from the most loosely bound to the most tightly bound particles on the electrode surfaces. First, electrons are emitted from the cathode after electric-field-induced breakdown. Then loosely bound protons are thermally emitted from the anode. As the temperature increase, neutral contaminants are desorbed from both electrodes and rapidly ionize. At inner radii, the metal eventually vaporizes.

Some portion of the surface plasmas thus formed is transported into the transmission-line gap under the force of the electric field, with aid from plasma instabilities. The gap plasmas then drift downstream with velocity equal to E/B, where they accumulate and contribute to a likely Hall-related cross-gap current.

While significant progress has been reported here, there are gaps remaining in our understanding that we have the tools in place to address. Questions include how much the current is lost in the convolute and through what processes, how are particles/plasma sourced, how may loss be mitigated, and how do losses scale to higher currents. While we have confirmed that electrode plasmas are responsible for current loss, measuring the precise inventory has a been a decades-long pursuit in power-flow physics. Using our unmatched simulation capability, we have identified experiments that are sensitive to the electrode contaminant inventory with existing probes. In addition, diagnostics are developed to measure ns-scale thermal desorption. Experiments designed to measure convolute losses, test new configurations, and scale to higher currents are scheduled for the coming years. A long-sought technique for mitigating current via *in situ* plasma cleaning, which is completing development on Mykonos for implementation on Z. Longer-term projects include measuring the emergence of vaporization and simulating its impact on plasma in the vicinity of diagnostic apertures and the z-pinch load.

The achievements in experimental execution, model validation, and physical analysis presented in this report set the stage for continued progress in power flow and load diagnostics on Z. The planned shot schedule for Z and Mykonos will provide data for extrapolation to higher current to ensure the efficiency of a NGPP facility.

REFERENCES

[1] R. Balescu. *Transport Processes in Plasmas*. North Holland, Amsterdam, 1988.

[2] J. T. Banasek, C. Goyon, S. C. Bott-Suzuki, G. F. Swadling, M. Quinley, B. Levitt, B. A. Nelson, U. Shumlak, and H. S. McLean. Probing local electron temperature and density inside a sheared flow stabilized Z-pinch using portable optical Thomson scattering. *Rev. Sci. Instru.*, 94(2):023508, 02 2023.

[3] N. Bennett, D. R. Welch, K. Cochrane, K. Leung, C. Thoma, M. E. Cuneo, and G. Frye-Mason. Electrode plasma formation and melt in z-pinch accelerators. *Phys. Rev. Accel. Beams*, 26:040401, Apr 2023.

[4] N. Bennett, D. R. Welch, C. A. Jennings, E. Yu, M. H. Hess, B. T. Hutsel, G. Laity, J. K. Moore, D. V. Rose, K. Peterson, and M. E. Cuneo. Current transport and loss mechanisms in the z accelerator. *Phys. Rev. Accel. Beams*, 22:120401, Dec 2019.

[5] N. Bennett, D. R. Welch, G. Laity, D. V. Rose, and M. E. Cuneo. Magnetized particle transport in multi-ma accelerators. *Phys. Rev. Accel. Beams*, 24:060401, Jun 2021.

[6] N. Bennett and D.R. Welch. Resolution requirements for energy conservation in kinetic plasma simulations. Technical Report SAND2022-13998, Sandia National Laboratories, 2022.

[7] C. K. Birdsall and A. B. Langdon. *Plasma Physics via Computer Simulation*. Adam Hilger, New York, 1991.

[8] J. P. Boris. *Relativistic plasma simulation – Optimization of a hybrid code*. Naval Research Laboratory, Washington DC, 1970.

[9] T.J.M. Boyd and J.J. Sanderson. *The Physics of Plasmas*. Cambridge University Press, 2003.

[10] S. I. Braginskii. Transport Processes in a Plasma. In M. A. Leontovich, editor, *Reviews of Plasma Physics*, volume 1, page 205. Consultants Bureau, New York, 1965.

[11] Nichelle Bruner, Thomas Genoni, Elizabeth Madrid, David Rose, Dale Welch, Kelly Hahn, Joshua Leckbee, Salvador Portillo, Bryan Oliver, Vernon Bailey, and David Johnson. Modeling particle emission and power flow in pulsed-power driven, nonuniform transmission lines. *Phys. Rev. ST Accel. Beams*, 11(4):040401, Apr 2008.

[12] Nichelle Bruner, Thomas Genoni, Elizabeth Madrid, Dale Welch, Kelly Hahn, and Bryan Oliver. Excitation of voltage oscillations in an induction voltage adder. *Phys. Rev. ST Accel. Beams*, 12(7):070401, Jul 2009.

[13] C. A. Coverdale, C. Deeney, A. L. Velikovich, J. Davis, R. W. Clark, Y. K. Chong, J. Chittenden, S. Chantrenne, C. L. Ruiz, G. W. Cooper, A. J. Nelson, J. Franklin, P. D. LePell, J. P. Apruzese, J. Levine, and J. Banister. Deuterium gas-puff z-pinch implosions on the z accelerator. *Phys. Plasmas*, 14(5):–, 2007.

[14] J. M. Creedon. Relativistic brillouin flow in the high ν/γ diode. *J. Appl. Phys.*, 46:2946, 1975.

[15] J. M. Creedon. Magnetic cutoff in high-current diodes. *J. Appl. Phys.*, 48:1070, 1977.

[16] M. E. Cuneo, P. R. Menge, D.L. Hanson, W.E. Fowler, M.A Bernard, G.R. Ziska, AB. Filuk, T.D. Pointon, R.A Vesey, D.R. Welch, James E. Bailey, M.P. Desjarlais, T.R. Lockner, T.A Mehlhorn, S.A Slutz, and M.A Stark. Results of vacuum cleaning techniques on the performance of lif field-threshold ion sources on extraction applied-b ion diodes at 1-10 tw. *IEEE Trans. Plasma Sci.*, 25(2):229–251, Apr 1997.

[17] M.E. Cuneo. The effect of electrode contamination, cleaning and conditioning on high-energy pulsed-power device performance. *IEEE Transactions on Dielectrics and Electrical Insulation*, 6(4):469–485, 1999.

[18] D. H. Dolan. Accuracy and precision in photonic Doppler velocimetry. *Rev. Sci. Instru.*, 81(5), 05 2010.

[19] D. H. Dolan. Extreme measurements with photonic doppler velocimetry (pdv). *Review of Scientific Instruments*, 91(5):051501, 2020.

[20] D. H. Dolan, K. Bell, B. Fox, S. C. Jones, P. Knapp, M. R. Gomez, M. Martin, A. Porwitzky, and G. Laity. Plasma and radiation detection via fiber interferometry. *J. Appl. Phys.*, 123(3):034502, 2018.

[21] R.H. Fowler and L. Nordheim. Electron emission in intense electric fields. *Proc. Royal Society London, A*, 119:173–181, 1928.

[22] T. C. Genoni, R. E. Clark, and D. R. Welch. A fast implicit algorithm for highly magnetized charged particle motion. *The Open Plasma Physics Journal*, 3:36, 2010.

[23] B. B. Godfrey. Time-biased field solver for electromagnetic codes. Technical Report AMRC-N-138, Mission Research Corp., 1980. Presented at the 9th Conference on the Numerical Simulation of Plasmas.

[24] M. R. Gomez, R. M. Gilgenbach, M. E. Cuneo, C. A. Jennings, R. D. McBride, E. M. Waisman, B. T. Hutsel, W. A. Stygar, D. V. Rose, and Y. Maron. Experimental study of current loss and plasma formation in the *z* machine post-hole convolute. *Phys. Rev. Accel. Beams*, 20:010401, Jan 2017.

[25] N. Hines. Development of a colinear second-harmonic orthogonal polarization (SHOP) interferometer for line-averaged electron density measurements in magnetically insulated transmission lines. Technical Report SAND2023-nnnn, Sandia National Laboratories, 2023.

[26] D.D. Hinshelwood. Bertha– A versatile transmission line and circuit code. *Naval Research Laboratory, Washington, DC, Memo. Rep. 5185*, Nov. 1983.

[27] Thomas P. Hughes, Robert E. Clark, and Simon S. Yu. Three-dimensional calculations for a 4 kA, 3.5 MV, 2 microsecond injector with asymmetric power feed. *Phys. Rev. ST Accel. Beams*, 2(11):110401, Nov 1999.

[28] T.P. Hughes and L.C. Musson. Shperical expansion of a dense plasma: test of ambipolar field model in aleph. Technical Report SAND2014-19336, Sandia National Laboratories, 2014.

[29] B. T. Hutsel, P. A. Corcoran, M. E. Cuneo, M. R. Gomez, M. H. Hess, D. D. Hinshelwood, C. A. Jennings, G. R. Laity, D. C. Lamppa, R. D. McBride, J. K. Moore, A. Myers, D. V. Rose, S. A. Slutz, W. A. Stygar, E. M. Waisman, D. R. Welch, and B. A. Whitney. Transmission-line-circuit model of an 85-tw, 25-ma pulsed-power accelerator. *Phys. Rev. Accel. Beams*, 21:030401, Mar 2018.

[30] C. A. Jennings, D. J. Ampleford, D. C. Lamppa, S. B. Hansen, B. Jones, A. J. Harvey-Thompson, M. Jobe, T. Strizic, J. Reneker, G. A. Rochau, and M. E. Cuneo. Computational modeling of krypton gas puffs with tailored mass density profiles on z. *Phys. Plasmas*, 22(5):056316, 2015.

[31] M. C. Jones, D. J. Ampleford, M. E. Cuneo, R. Hohlfelder, C. A. Jennings, D. W. Johnson, B. Jones, M. R. Lopez, J. MacArthur, J. A. Mills, T. Preston, G. A. Rochau, M. Savage, D. Spencer, D. B. Sinars, and J. L. Porter. X-ray power and yield measurements at the refurbished Z machine. *Rev. Sci. Instru.*, 85(8), 08 2014.

[32] A. A. Kim, M. G. Mazarakis, V. A. Sinebryukhov, B. M. Kovalchuk, V. A. Visir, S. N. Volkov, F. Bayol, A. N. Bastrikov, V. G. Durakov, S. V. Frolov, V. M. Alexeenko, D. H. McDaniel, W. E. Fowler, K. LeChien, C. Olson, W. A. Stygar, K. W. Struve, J. Porter, and R. M. Gilgenbach. Development and tests of fast 1-ma linear transformer driver stages. *Phys. Rev. ST Accel. Beams*, 12:050402, May 2009.

[33] H. Knoepfel. *Magnetic Fields*. John Wiley and Sons, New York, 2000.

[34] G. Laity, M. Johnston, S. Patel, and M. Cuneo. Power flow spectroscopy diagnostics & platorm development at the Z pulsed power facility. Technical Report SAND2020-11144R, Sandia National Laboratories, 2020.

[35] George R. Laity, Allen C. Robinson, Michael E. Cuneo, M. Kathleen Alam, Kristian R. C. Beckwith, Nichelle L. Bennett, Matthew T. Bettencourt, Stephen D. Bond, Kyle Cochrane, Louise Criscenti, Eric C. Cyr, Karen De Zetter, Richard R. Drake, Evstati G. Evstatiev, Andrew S. Fierro, Thomas A. Gardiner, Forrest W. Glinesa, Ronald S. Goeke, Nathaniel D. Hamlin, Russell Hooper, Jason Koski, J. Matthew Lane, Steven R. Larson, Kevin Leung, Duncan A. McGregor, Philip R. Miller, Sean M. Miller, Susan J. Ossareh, Edward G. Phillips, Nicholas A. Roberds, Charles E. Rose, John N. Shadid, Sidney Shields, Sean C. Simpson, David Sirajuddina, Thomas M. Smith, M. Scot Swan, Aidan P. Thompson, and Julien G. Tranchida. Towards predictive plasma science and engineering through revolutionary multi-scale algorithms and models, final report. Technical Report SAND2021-0718, Sandia National Laboratories, 2021.

[36] D. Lamppa, D.V. Rose, G. Shipley B.T. Hutsel, J. Schwarz, and M.E. Cuneo. A diagnostically accessible scaling platform for observing electrode plasma formation in > 1 MA/cm MITLs. In *Proc. of Pulsed Power Conference 2023*. IEEE, 2023.

[37] I. Langmuir. The effect of space charge and residual gases on thermionic currents in high vacuum. *Phys. Rev.*, 2:450, 1913.

[38] Robert I. Lawconnell and Jesse Neri. Theory of magnetically insulated electron flows in coaxial pulsed power transmission lines. *Phys. Fluids B*, 2(3):629–639, 1990.

[39] W.R. Leo. *Techniques for Nuclear and Particle Physics Experiments*. Springer-Verlag, New York Berlin Heidelberg, second edition, 1994.

[40] Kevin Leung, Ronald S. Goeke, Anastasia G. Ilgen, Alexander Wilson, Michael E. Cuneo, and Nichelle Bennett. Examining the molecular origins of anomalously high H_2O generation at oxide-passivated metal surfaces for plasma applications. *J. Phys.: Condens. Matter*, 35(45):455001, Aug 2023.

[41] J. J. MacFarlane, I. E. Golovkin, P. Wang, P. R. Woodruff, and N. A. Pereyra. SPECT3D – A multi-dimensional collisional-radiative code for generating diagnostic signatures based on hydrodynamics and PIC simulation output. *High Energy Dens. Phys.*, 3(1):181–190, May 2007.

[42] E. A. Madrid, D. V. Rose, D. R. Welch, R. E. Clark, C. B. Mostrom, W. A. Stygar, M. E. Cuneo, M. R. Gomez, T. P. Hughes, T. D. Pointon, and D. B. Seidel. Steady-state modeling of current loss in a post-hole convolute driven by high power magnetically insulated transmission lines. *Phys. Rev. ST Accel. Beams*, 16:120401, Dec 2013.

[43] C. W. Mendel. Planar one-dimensional magnetically insulated electron flow for arbitrary canonical-momentum distribution. *J. Appl. Phys.*, 50:3830, 1979.

[44] E. L. Murphy and R. H. Good. Thermionic emission, field emission, and the transition region. *Phys. Rev.*, 102:1464–1473, Jun 1956.

[45] C. E. Myers. Using scaled power flow experiments at 20 ma to establish the efficacy of load current delivery on a $>$ 50 ma next-generation pulsed power facility. In *APS Division of Plasma Physics Meeting Abstracts*, volume 2021 of *APS Meeting Abstracts*, Nov. 2021.

[46] Clayton E. Myers, Derek C. Lamppa, Christopher A. Jennings, Matthew R. Gomez, Patrick F. Knapp, Michael R. Kossow, Larry M. Lucero, James K. Moore, and David A. Yager-Elorriaga. The inductively driven transmission line: A passively coupled device for diagnostic applications on the Z pulsed power facility. *Rev. Sci. Instru.*, 92(3), 03 2021.

[47] T. D. Pointon, W. A. Stygar, R. B. Spielman, H. C. Ives, and K. W. Struve. Particle-in-cell simulations of electron flow in the post-hole convolute of the z accelerator. *Phys. Plasmas*, 8(10):4534–4544, 2001.

[48] A. Porwitzky, D. H. Dolan, M. R. Martin, G. Laity, R. W. Lemke, and T. R. Mattsson. Direct measurements of anode/cathode gap plasma in cylindrically imploding loads on the z machine. *Phys. Plasmas*, 25(6):063110, 2018.

[49] Andrew Porwitzky, Brian T. Hutsel, Christopher T. Seagle, Tommy Ao, Sean Grant, Aaron Bernstein, Jung-Fu Lin, and Todd Ditmire. Large time-varying inductance load for studying power flow on the *z* machine. *Phys. Rev. Accel. Beams*, 22:090401, Sep 2019.

[50] P. D. Prewett, J. E. Allen, and Douglas William Holder. The double sheath associated with a hot cathode. *Proc. Royal Society London, A*, 348(1655):435–446, 1976.

[51] P.A. Redhead. *The Physical Basis for Ultrahigh Vacuum*. Chapman and Hall, London, 1968.

[52] A. S. Richardson, J. C. Zier, J. T. Engelbrecht, S. B. Swanekamp, J. W. Schumer, D. Mosher, P. F. Ottinger, D. L. Duke, T. J. Haines, M. P. McCumber, and A. Gehring. Simulations of the generation and transport of a 5 mv end-point x-ray beam on a pulsed power generator. *Phys. Rev. Accel. Beams*, 22:050401, May 2019.

[53] D. V. Rose, E. A. Madrid, D. R. Welch, R. E. Clark, C. B. Mostrom, W. A. Stygar, and M. E. Cuneo. Computational analysis of current-loss mechanisms in a post-hole convolute driven by magnetically insulated transmission lines. *Phys. Rev. ST Accel. Beams*, 18:030402, Mar 2015.

[54] D. V. Rose, C. L. Miller, D. R. Welch, R. E. Clark, E. A. Madrid, C. B. Mostrom, W. A. Stygar, K. R. LeChien, M. A. Mazarakis, W. L. Langston, J. L. Porter, and J. R. Woodworth. Circuit models and three-dimensional electromagnetic simulations of a 1-ma linear transformer driver stage. *Phys. Rev. ST Accel. Beams*, 13(9):090401, Sep 2010.

[55] D. V. Rose, E. M. Waisman, M. P. Desjarlais, M. E. Cuneo, B. T. Hutsel, D. R. Welch, N. Bennett, and G. R. Laity. Numerical simulations of enhanced ion current losses in the inner magnetically insulated transmission line of the *z* accelerator. *Phys. Rev. Accel. Beams*, 23:080401, Aug 2020.

[56] D. V. Rose, D. R. Welch, T. P. Hughes, R. E. Clark, and W. A. Stygar. Plasma evolution and dynamics in high-power vacuum-transmission-line post-hole convolutes. *Phys. Rev. ST Accel. Beams*, 11:060401, Jun 2008.

[57] D. V. Rose, D. R. Welch, E. A. Madrid, C. L. Miller, R. E. Clark, W. A. Stygar, M. E. Savage, G. A. Rochau, J. E. Bailey, T. J. Nash, M. E. Sceiford, K. W. Struve, P. A. Corcoran, and B. A. Whitney. Three-dimensional electromagnetic model of the pulsed-power *z*-pinch accelerator. *Phys. Rev. ST Accel. Beams*, 13:010402, 2010.

[58] T. W. L. Sanford, J. A. Halbleib, J. W. Poukey, A. L. Pregenzer, R. C. Pate, C. E. Heath, R. Mock, G. A. Mastin, D. C. Ghiglia, T. J. Roemer, P. W. Spence, and G. A. Proulx. Measurement of electron energy deposition necessary to form an anode plasma in Ta, Ti, and C for coaxial bremsstrahlung diodes. *J. Appl. Phys.*, 66(1):10–22, 1989.

[59] M. E. Savage, K. R. LeChien, M. R. Lopez, B. S. Stoltzfus, W. A. Stygar, D. S. Artery, J. A. Lott, and P. A. Corcoran. Status of the z pulsed power driver. In *2011 IEEE Pulsed Power Conference*, pages 983–990, 2011.

[60] D. B. Sinars, M. A. Sweeney, C. S. Alexander, D. J. Ampleford, T. Ao, J. P. Apruzese, C. Aragon, D. J. Armstrong, K. N. Austin, T. J. Awe, A. D. Baczewski, J. E. Bailey, K. L. Baker, C. R. Ball, H. T. Barclay, S. Beatty, K. Beckwith, K. S. Bell, J. F. Benage, N. L. Bennett, K. Blaha, D. E. Bliss, J. J. Boerner, C. J. Bourdon, B. A. Branch, J. L. Brown, E. M. Campbell, R. B. Campbell, D. G. Chacon, G. A. Chandler, K. Chandler, P. J. Christenson, M. D. Christison, E. B. Christner, R. C. Clay, K. R. Cochrane, A. P. Colombo, B. M. Cook, C. A. Coverdale, M. E. Cuneo, J. S. Custer, A. Dasgupta, J.-P. Davis, M. P. Desjarlais, D. H. Dolan, J. D. Douglass, G. S. Dunham, S. Duwal, A. D. Edens, M. J. Edwards, E. G. Evstatiev, B. G. Farfan, J. R. Fein, E. S. Field, J. A. Fisher, T. M. Flanagan, D. G. Flicker, M. D. Furnish, B. R. Galloway, P. D. Gard, T. A. Gardiner, M. Geissel, J. L. Giuliani, M. E. Glinsky, M. R. Gomez, T. Gomez, G. P. Grim, K. D. Hahn, T. A. Haill, N. D. Hamlin, J. H.

Hammer, S. B. Hansen, H. L. Hanshaw, E. C. Harding, A. J. Harvey-Thompson, D. Headley, M. C. Herrmann, M. H. Hess, C. Highstrete, O. A. Hurricane, B. T. Hutsel, C. A. Jennings, O. M. Johns, D. Johnson, M. D. Johnston, B. M. Jones, M. C. Jones, P. A. Jones, P. E. Kalita, R. J. Kamm, J. W. Kellogg, M. L. Kiefer, M. W. Kimmel, P. F. Knapp, M. D. Knudson, A. Kreft, G. R. Laity, P. W. Lake, D. C. Lamppa, W. L. Langston, J. S. Lash, K. R. LeChien, J. J. Leckbee, R. J. Leeper, G. T. Leifeste, R. W. Lemke, W. Lewis, S. A. Lewis, G. P. Loisel, Q. M. Looker, A. J. Lopez, D. J. Lucero, S. A. MacLaren, R. J. Magyar, M. A. Mangan, M. R. Martin, T. R. Mattsson, M. K. Matzen, A. J. Maurer, M. G. Mazarakis, R. D. McBride, H. S. McLean, C. A. McCoy, G. R. McKee, J. L. McKenney, A. R. Miles, J. A. Mills, M. D. Mitchell, N. W. Moore, C. E. Myers, T. Nagayama, G. Natoni, A. C. Owen, S. Patel, K. J. Peterson, T. D. Pointon, J. L. Porter, A. J. Porwitzky, S. Radovich, K. S. Raman, P. K. Rambo, W. D. Reinhart, G. K. Robertson, G. A. Rochau, S. Root, D. V. Rose, D. C. Rovang, C. L. Ruiz, D. E. Ruiz, D. Sandoval, M. E. Savage, M. E. Sceiford, M. A. Schaeuble, P. F. Schmit, M. S. Schollmeier, J. Schwarz, C. T. Seagle, A. B. Sefkow, D. B. Seidel, G. A. Shipley, J. Shores, L. Shulenburger, S. C. Simpson, S. A. Slutz, I. C. Smith, C. S. Speas, P. E. Specht, M. J. Speir, D. C. Spencer, P. T. Springer, A. M. Steiner, B. S. Stoltzfus, W. A. Stygar, J. Ward Thornhill, J. A. Torres, J. P. Townsend, C. Tyler, R. A. Vesey, P. E. Wakeland, T. J. Webb, E. A. Weinbrecht, M. R. Weis, D. R. Welch, J. L. Wise, M. Wu, D. A. Yager-Elorriaga, A. Yu, and E. P. Yu. Review of pulsed power-driven high energy density physics research on z at sandia. *Phys. Plasmas*, 27(7):070501, 2020.

[61] Boris V. Somov. *Plasma Astrophysics: Part I Fundamentals and Practice*. Springer Science+Business Media, LLC, 2006.

[62] R. B. Spielman, C. Deeney, G. A. Chandler, M. R. Douglas, D. L. Fehl, M. K. Matzen, D. H. McDaniel, T. J. Nash, J. L. Porter, T. W. L. Sanford, J. F. Seamen, W. A. Stygar, K. W. Struve, S. P. Breeze, J. S. McGurn, J. A. Torres, D. M. Zagar, T. L. Gilliland, D. O. Jobe, J. L. McKenney, R. C. Mock, M. Vargas, T. Wagoner, and D. L. Peterson. Tungsten wire-array z-pinch experiments at 200 tw and 2 mj. *Phys. Plasmas*, 5(5):2105–2111, 1998.

[63] W. A. Stygar, P. A. Corcoran, H. C. Ives, R. B. Spielman, J. W. Douglas, B. A. Whitney, M. A. Mostrom, T. C. Wagoner, C. S. Speas, T. L. Gilliland, G. A. Allshouse, R. E. Clark, G. L. Donovan, T. P. Hughes, D. R. Humphreys, D. M. Jaramillo, M. F. Johnson, J. W. Kellogg, R. J. Leeper, F. W. Long, T. H. Martin, T. D. Mulville, M. D. Pelock, B. P. Peyton, J. W. Poukey, J. J. Ramirez, P. G. Reynolds, J. F. Seamen, D. B. Seidel, A. P. Seth, A. W. Sharpe, R. W. Shoup, J. W. Smith, D. M. Van De Valde, and R. W. Wavrik. 55-tw magnetically insulated transmission-line system: Design, simulations, and performance. *Phys. Rev. ST Accel. Beams*, 12:120401, 2009.

[64] W. A. Stygar, H. C. Ives, D. L. Fehl, M. E. Cuneo, M. G. Mazarakis, J. E. Bailey, G. R. Bennett, D. E. Bliss, G. A. Chandler, R. J. Leeper, M. K. Matzen, D. H. McDaniel, J. S. McGurn, J. L. McKenney, L. P. Mix, D. J. Muron, J. L. Porter, J. J. Ramirez, L. E. Ruggles, J. F. Seamen, W. W. Simpson, C. S. Speas, R. B. Spielman, K. W. Struve, J. A. Torres, R. A. Vesey, T. C. Wagoner, T. L. Gilliland, M. L. Horry, D. O. Jobe, S. E. Lazier, J. A. Mills, T. D. Mulville, J. H. Pyle, T. M. Romero, J. J. Seamen, and R. M. Smelser. X-ray emission from z pinches at 10^7 a: Current scaling, gap closure, and shot-to-shot fluctuations. *Phys. Rev. E*, 69:046403, Apr 2004.

[65] C. Thoma, D.R. Welch, N. Bennett, and K. Cochrane. Improved melt model for power flow. Technical Report SAND2023-09787R, Sandia National Laboratories, 2023.

[66] K. Tummel, D. R. Welch, D. V. Rose, A. J. Link, and K. R. LeChien. Impact of power flow on Z-pinch loads. *Phys. Plasmas*, 29(11):113102, 11 2022.

[67] E. Waisman. Current loss in convolute and inner mitl. unpublished, 2021.

[68] Eduardo M. Waisman, M. P. Desjarlais, and M. E. Cuneo. Ion current losses in the convolute and inner magnetically insulated transmission line of the *z* machine. *Phys. Rev. Accel. Beams*, 22:030402, Mar 2019.

[69] T. J. Webb, D. E. Bliss, G. A. Chandler, D. H. Dolan, G. Dunham, A. Edens, E. Harding, M. D. Johnston, M. C. Jones, S. Langendorf, M. Mangan, A. J. Maurer, C. A. McCoy, N. W. Moore, R. Presura, A. M. Steiner, M. Wu, D. A. Yager-Elorriaga, and K. C. Yates. Radiation, optical, power flow, and electrical diagnostics at the Z facility: Layout and techniques utilized to operate in the harsh environment. *Rev. Sci. Instru.*, 94(3), 03 2023. 031102.

[70] M. R. Weis, A. J. Harvey-Thompson, and D. E. Ruiz. Scaling laser preheat for maglif with the z-beamlet laser. *Phys. Plasmas*, 28(1):012705, 2021.

[71] D. R. Welch, N. Bennett, T. C. Genoni, D. V. Rose, C. Thoma, C. Miller, and W. A. Stygar. Electrode contaminant plasma effects in 10^7-ampere z pinch accelerators. *Phys. Rev. Accel. Beams*, 22:070401, 2019.

[72] D. R. Welch, N. Bennett, T. C. Genoni, C. Thoma, and D. V. Rose. Fast hybrid particle-in-cell technique for pulsed-power accelerators. *Phys. Rev. Accel. Beams*, 23:110401, Nov 2020.

[73] D.R. Welch, T.C. Genoni, R.E. Clark, and D.V. Rose. Adaptive particle management in a particle-in-cell code. *J. Comp. Phys.*, 227(1):143 – 155, 2007.

[74] D. A. Yager-Elorriaga, M. M. Montoya, D. E. Bliss, C. R. Ball, P. Atencio, B. C. Carpenter, K. Fuerschbach, K. W. Fulford, D. C. Lamppa, M. C. Lowinske, L. Lucero, A. J. Maurer, S. Patel, A. Romero, D. J. Scoglietti, A. Tanbakuchi, and A. J. York. Optical imaging on Z LDRD: Design and developmentof self-emission and debris imagers. Technical Report SAND2021-12610, Sandia National Laboratories, 2021.

[75] D. Zimmer, F. Conti, F. Beg, M.R. Gomez, C.A. Jennings, C.E. Myers, and N. Bennett. How an applied axial magnetic field impacts efficient current coupling on the z machine. *submitted to Phys. Rev. Accel. Beams*, 2023.

APPENDIX A. VERIFICATION PROBLEMS FOR POWER FLOW CODES

Power flow simulations for Z, and at the multi-MA scale generally, must resolve charged particle motion for pulse duration of hundreds of ns and over length scales up to tens of cm in 2D and 3D. Parallelized codes with domain decomposition are one accommodation to the length scales, but the codes should under-resolve the Debye length. This is to reduce the number of cells or elements in a simulation and also to increase the time step, which is limited by the element sizes through the Courant condition. Simulation time steps must also resolve particle motion (cyclotron orbits, collisions, charge separation, etc) or prove under-resolution is viable [71]. Finally, this potential under-resolution must demonstrate energy and momentum conservation to approximately 1%.

The 1D expanding-plasma verification problem described here stresses the energy conservation of traditional PIC techniques while under resolving the Debye length by a factor of 20. The analytic theory of Hughes and Musson [28] at steady state is used to test simulations of both neutral gas and plasma. Specifically, the problem tests the accuracy of the conversion of thermal energy into kinetic or fluid motion in both kinetic and two fluid treatments. A test of the CHICAGO Magnetic Implicit algorithm illustrates the concept.

Hughes and Musson [28] derived a 1D spherical steady state expression of the conversion of thermal energy into "fluid" motion for warm electron (temperature T_e) and cold ion (mass m_i) populations with an ambipolar field. The dimensionless velocity, position and density are given by

$$\begin{aligned} \hat{v}(r) &= \frac{v(r)}{v(1)} = \frac{v(r)}{c_s}, \\ \hat{r} &= \frac{r}{r(1)} = \sqrt{\frac{1}{\hat{v}}}\exp\frac{\hat{v}^2-1}{4}, \\ \hat{n} &= \frac{n}{n(1)} = \frac{\hat{n}(1)}{\hat{r}^2\hat{v}} \end{aligned} \tag{9}$$

where $c_s = \sqrt{kT_e/m_i}$ is the sound speed. The equation for $\hat{v}$ is transcendental and must be iterated for solution. The problem is initiated at small radius (1 cm) with T_e and $v(1)$ and is followed for 10 μs as the particles expand to 10 cm as shown in Fig. 8-1. The ions and neutrals are assumed to have hydrogen mass. A simple Spitzer collision operator is used for ions and a hard sphere collision operator is used for neutral on neutral collisions.

Neutral Gas Expansion

As a first test, we inject neutral gas cold with $v = c_s$ (1 eV). In this case, the steady state solution simplifies to $\hat{n} = \hat{n}(1)/\hat{r}^2$. In a second test, the neutrals are injected with no net velocity and 1 eV temperature. The 1 eV gas expands to roughly $v = c_s$ (3 eV) and the density falls more rapidly as seen in Fig. 8-2. The Hughes and Musson theory and CHICAGO simulation results are shown for the two example cases and agree quite well.

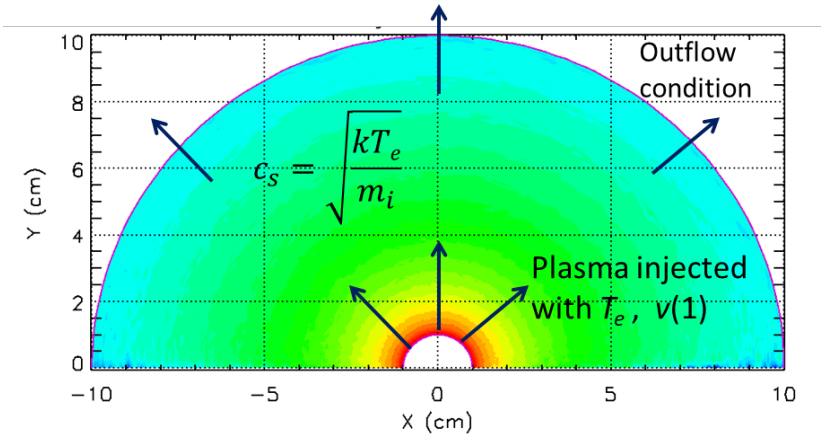

Figure 8-1 The spherical geometry for the steady state theory and simulations.

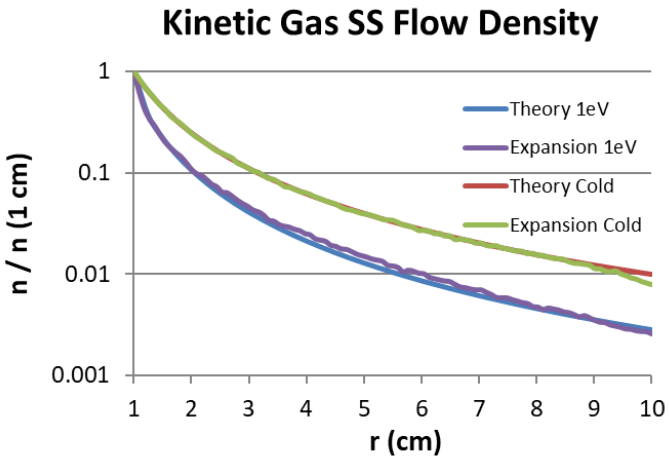

Figure 8-2 Steady state gas density with initial conditions of 1 eV and cold with v (1 cm)=c_s (1 eV), shown for both CHICAGO simulation and analytical theory.

Plasma Expansion with Kinetic and Two-Fluid Simulations

In this section, we include charged particles and an electrostatic field solution to model a 2.0e11 cm^{-3} e- H+ plasma with a $v(1\text{ cm}) = c_s$ (1 eV) = 9.82e5 cm/s. We use CHICAGO's energy-conserving implicit technique with fully kinetic and two-fluid (Eulerian) particle treatments in 2D (r, θ) spherical geometry. We use 100 cells in θ over the entire π range. In radius, we use 180 cells or 0.05-cm uniform cell size. Note that the plasma collisionless skin depth is 1.2 cm and the Debye length is 0.0017 cm - under resolved by 20 in the simulation. Thus, this is an excellent test of the energy conserving technique. The time step (0.018 ns) adequately resolves the plasma frequency ($\omega_p \Delta t = 0.42$) so the implicit technique is not actually needed. We inject 1 particle/step per transverse cell yielding 5 million macroparticles for electrons and ions. In Fig. 8-3, we plot the Hughes and Musson theory and CHICAGO simulation results after 10 μs

using both the fully kinetic and two-fluid treatments; excellent agreement is observed.

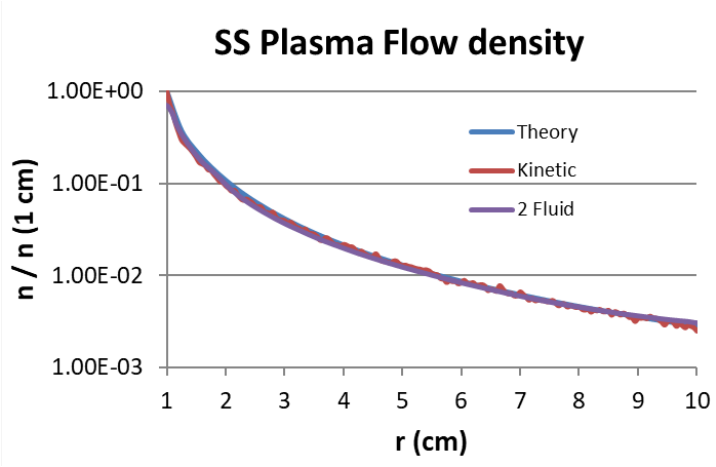

Figure 8-3 Steady state plasma densities for an initial condition of $T_e = 1$ eV, $v = c_s$ (1 eV), for both CHICAGO kinetic and two-fluid treatments, as well as analytical theory.

DISTRIBUTION

Email—Internal

Name	Org.	Sandia Email Address
Michael Cuneo	1650	mecuneo@sandia.gov
Jens Schwarz	1659	jschwar@sandia.gov
Nichelle Bennett	1684	nlbenne@sandia.gov
Derek Lamppa	1659	dclampp@sandia.gov
Andrew Porwitzky	1641	ajporwi@sandia.gov
Christopher Jennings	1684	cjennin@sandia.gov
Evstati Evstatiev	1684	egevsta@sandia.gov
Jacob Banasek	1659	jtbabas@sandia.gov
Sonal Patel	6772	spatel@sandia.gov
Katherine Chandler	1683	kchandl@sandia.gov
Mark Savage	1651	mesavag@sandia.gov
David Yager-Elorriaga	1683	dayager@sandia.gov
Mark Johnston	1391	mdjohn@sandia.gov
Mark Hess	1684	mhess@sandia.gov
Technical Library	1911	sanddocs@sandia.gov

Email—External

Name	Company Email Address	Company Name
Dale Welch	dalew@vosssci.com	Voss Scientific, LLC
David Rose	davidr@vosssci.com	Voss Scientific, LLC
Eric Watson	ericw@vosssci.com	Voss Scientific, LLC

Hardcopy—Internal

Number of Copies	Name	Org.	Mailstop

Sandia National Laboratories

Sandia National Laboratories is a multimission laboratory managed and operated by National Technology & Engineering Solutions of Sandia LLC, a wholly owned subsidiary of Honeywell International Inc., for the U.S. Department of Energy's National Nuclear Security Administration under contract DE-NA0003525.